

Staggered Schemes for Fluctuating Hydrodynamics

Florencio Balboa,¹ John B. Bell,² Rafael Delgado-Buscalioni,¹ Aleksandar Donev,^{3,*} Thomas Fai,³ Boyce Griffith,⁴ and Charles S. Peskin³

¹*Departamento de Física Teórica de la Materia Condensada,
Univeridad Autónoma de Madrid, Madrid 28049, Spain*

²*Center for Computational Science and Engineering,
Lawrence Berkeley National Laboratory, Berkeley, CA, 94720*

³*Courant Institute of Mathematical Sciences,
New York University, New York, NY 10012*

⁴*Leon H. Charney Division of Cardiology, Department of Medicine,
New York University School of Medicine, New York, NY 10016*

We develop numerical schemes for solving the isothermal compressible and incompressible equations of fluctuating hydrodynamics on a grid with staggered momenta. We develop a second-order accurate spatial discretization of the diffusive, advective and stochastic fluxes that satisfies a discrete fluctuation-dissipation balance, and construct temporal discretizations that are at least second-order accurate in time deterministically and in a weak sense. Specifically, the methods reproduce the correct equilibrium covariances of the fluctuating fields to third (compressible) and second (incompressible) order in the time step, as we verify numerically. We apply our techniques to model recent experimental measurements of giant fluctuations in diffusively mixing fluids in a micro-gravity environment [*A. Vailati et. al., Nature Communications 2:290, 2011*]. Numerical results for the static spectrum of non-equilibrium concentration fluctuations are in excellent agreement between the compressible and incompressible simulations, and in good agreement with experimental results for all measured wavenumbers.

*Electronic address: donev@courant.nyu.edu

I. INTRODUCTION

At a molecular scale, fluids are not deterministic; the state of the fluid is constantly changing and stochastic, even at thermodynamic equilibrium. Stochastic effects are important for flows in new microfluidic, nanofluidic and microelectromechanical devices [1]; novel materials such as nanofluids [2]; biological systems such as lipid membranes [3], Brownian molecular motors [4], nanopores [5]; as well as processes where the effect of fluctuations is amplified by strong non-equilibrium effects, such as combustion of lean flames, capillary dynamics [6, 7], and hydrodynamic instabilities [8–10], and others. Because they span the whole range of scales from the microscopic to the macroscopic [11, 12], fluctuations need to be consistently included in all levels of description [13]. Thermal fluctuations are included in the Landau-Lifshitz Navier-Stokes (LLNS) equations and related continuum Langevin models [14, 15] through stochastic forcing terms, as first proposed by Landau and Lifshitz [16]. Numerically solving the continuum equations of *fluctuating hydrodynamics* [17] is difficult because of the presence of non-trivial dynamics at all scales and the existence of a nontrivial invariant measure (equilibrium distribution).

Several numerical approaches for fluctuating hydrodynamics have been proposed. The earliest work by Garcia *et al.* [18] developed a simple scheme for the stochastic heat equation and the linearized one-dimensional LLNS equations. Ladd and others have included stress fluctuations in (isothermal) Lattice Boltzmann methods for some time [19]. Moseler and Landman [8] included the stochastic stress tensor of the LLNS equations in the lubrication equations and obtain good agreement with their molecular dynamics simulation in modeling the breakup of nanojets. Sharma and Patankar [20] developed a fluid-structure coupling between a fluctuating incompressible solver and suspended Brownian particles. Coveney, De Fabritiis, Delgado-Buscalioni and co-workers have also used the isothermal LLNS equations in a hybrid scheme, coupling a continuum fluctuating solver to a molecular dynamics simulation of a liquid [21–23]. Atzberger, Kramer and Peskin have developed a version of the immersed boundary method that includes fluctuations [24, 25]. Voulgarakis and Chu [26] developed a staggered scheme for the isothermal compressible equations as part of a multi-scale method for biological applications, and a similar staggered scheme was also described in Ref. [27].

Some of us have recently developed techniques for analyzing the weak accuracy of finite-

volume methods for solving stochastic partial differential equations of the LLNS kind [28]. The analysis emphasizes the necessity to maintain fluctuation-dissipation balance in spatio-temporal discretizations [28], thus reproducing the Gibbs-Boltzmann distribution dictated by equilibrium statistical mechanics. Based on previous work by Bell *et al.* [29, 30], a collocated spatial discretization for the compressible equations of fluctuating hydrodynamics has been developed and combined with a stochastic third-order Runge-Kutta (RK3) temporal integrator [28]. The collocated spatial discretization has been used to construct a strictly conservative particle-continuum hybrid method [13] and to study the contribution of advection by thermal velocities to diffusive transport [31].

A staggered spatial discretization is advantageous for incompressible flows because it leads to a robust idempotent discrete projection operator [32, 33]. Staggered schemes have previously been developed for isothermal compressible [26] and incompressible flow [20], without, however, carefully assessing discrete fluctuation-dissipation balance. Here we present and test an explicit compressible and a semi-implicit incompressible scheme for fluctuating hydrodynamics on uniform staggered grids. Both methods use closely-related spatial discretizations. We ensure an accurate spectrum of the steady-state fluctuations by combining a locally-conservative finite-volume formulation, a non-dissipative (skew-symmetric) advection discretization, discretely dual divergence and gradient operators, and, in the case of incompressible flow, an unsplit Stokes solver preconditioned by a projection method.

Thermal fluctuations in non-equilibrium systems in which a constant (temperature, concentration, velocity) gradient is imposed externally exhibit remarkable behavior compared to equilibrium systems. Most notably, external gradients can lead to *enhancement* of thermal fluctuations and to *long-range* correlations between fluctuations [17, 34–37]. This phenomenon can be illustrated by considering concentration fluctuations in an isothermal mixture of two miscible fluids in the presence of a strong concentration gradient ∇c , as in the early stages of diffusive mixing between initially separated fluid components. As illustrated in Fig. 1, the interface between the fluids, instead of remaining flat, develops large-scale roughness that reaches a pronounced maximum until gravity or boundary effects intervene. These *giant fluctuations* [38–40] during free diffusive mixing have been observed using light scattering and shadowgraphy techniques [12, 41–44], finding good but imperfect agreement between the predictions of a simplified fluctuating hydrodynamic theory and experiments. Recent experiments have taken advantage of the enhancement of the nonequilibrium fluctuation

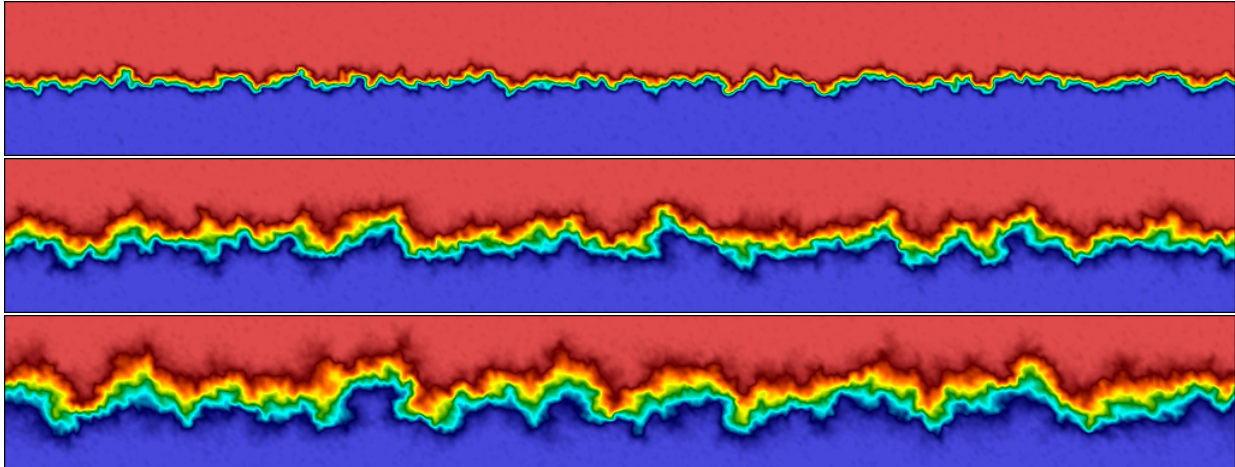


Figure 1: Snapshots of concentration showing the development of a *rough* diffusive interface between two miscible fluids in zero gravity. We show three points in time (top to bottom), starting from an initially perfectly flat interface (phase separated system). These figures were obtained using the incompressible code described in Section IV A.

tuations in a microgravity environment aboard the FOTON M3 spaceship [12, 43], and demonstrated the appearance of fractal diffusive fronts like those illustrated in Fig. 1. In the absence of gravity, the density mismatch between the two fluids does not change the qualitative nature of the non-equilibrium fluctuations, and in this work we focus on mixtures of dynamically-identical fluids.

Before discussing spatio-temporal discretizations, we review the continuum formulation of the equations of fluctuating hydrodynamics and their crucial properties in Section II. In particular, we discuss the steady-state covariances of the fluctuating fields for systems in thermal equilibrium as well as fluid mixtures with an imposed concentration gradient. In Section III A we focus on the temporal discretization in the spirit of the method of lines. For the compressible equations, we employ a previously-developed explicit three-stage Runge-Kutta scheme that is third order weakly accurate [28]. For the incompressible equations we employ a second-order accurate predictor-corrector approach, each stage of which is a semi-implicit (Crank-Nicolson) discretization of the Stokes equations, solved effectively using a projection method as a preconditioner [45]. In Section III B 5 we describe a conservative staggered spatial discretization of the diffusive, stochastic and advective fluxes. We maintain discrete fluctuation-dissipation balance [28, 46] by ensuring duality between the discrete divergence and gradient operators, and by using a skew-adjoint discretization of advection.

We verify the weak order of accuracy for both the compressible and incompressible algorithms in Section IV. In Section V we model the non-equilibrium concentration fluctuations in a fluid mixture under an applied temperature gradient, and compare the numerical results to recent experimental measurements [12, 43].

II. FLUCTUATING HYDRODYNAMICS

At mesoscopic scales the hydrodynamic behavior of fluids can be described with continuum stochastic PDEs of the Langevin type [14, 15], and in particular, the Landau-Lifshitz Navier-Stokes (LLNS) equations of fluctuating hydrodynamics [16, 47]. We consider fluctuating hydrodynamics for an ideal solution of a macromolecule with molecular mass M , and neglect gravity, barodiffusion, and fluctuations of the local temperature T , to obtain the fixed-temperature *compressible* LLNS equations for the density ρ , velocity \mathbf{v} , and mass concentration $c = \rho_1/\rho$ [17, 30]

$$D_t \rho = -\rho (\nabla \cdot \mathbf{v}) \quad (1)$$

$$\rho (D_t \mathbf{v}) = -\nabla P + \nabla \cdot [\eta \overline{\nabla \mathbf{v}} + \zeta (\nabla \cdot \mathbf{v}) \mathbf{I} + \Sigma] \quad (2)$$

$$\rho (D_t c) = \nabla \cdot [\rho \chi (\nabla c + c(1-c) S_T \nabla T) + \Psi], \quad (3)$$

supplemented with appropriate boundary conditions. Here $D_t \square = \partial_t \square + \mathbf{v} \cdot \nabla (\square)$ is the advective derivative, $\overline{\nabla \mathbf{v}} = (\nabla \mathbf{v} + \nabla \mathbf{v}^T) - 2(\nabla \cdot \mathbf{v}) \mathbf{I}/3$ is the symmetrized strain rate. We will assume that the pressure given by the equation of state is independent of concentration, $P(\rho, c; T) = P(\rho; T)$, justifying our neglect of barodiffusion. The shear viscosity η , bulk viscosity ζ , mass diffusion coefficient χ , and Soret coefficient S_T , can, in general, depend on the state.

The capital Greek letters denote stochastic fluxes that are modeled as white-noise random fields, with amplitudes determined from the fluctuation-dissipation balance principle [48]. For the compressible equations, there are many choices for how to express the stochastic stress, especially if additional bulk viscosity is included [49]. Since the physical implications of a particular choice are not well understood, we have based our implementation on a

formulation that requires no additional random numbers [47, 50],

$$\boldsymbol{\Sigma} = \sqrt{2\eta k_B T} \widetilde{\boldsymbol{\mathcal{W}}}_v + \left(\sqrt{\frac{\zeta k_B T}{3}} - \frac{\sqrt{2\eta k_B T}}{3} \right) \text{Tr}(\widetilde{\boldsymbol{\mathcal{W}}}_v) \mathbf{I}, \quad (4)$$

$$\boldsymbol{\Psi} = \sqrt{2\chi\rho M c(1-c)} \boldsymbol{\mathcal{W}}_c \quad (5)$$

where $\widetilde{\boldsymbol{\mathcal{W}}}_v = (\boldsymbol{\mathcal{W}}_v + \boldsymbol{\mathcal{W}}_v^T)/\sqrt{2}$ is a symmetric Gaussian random tensor field, and the $\sqrt{2}$ in the denominator accounts for the reduction in variance due to the averaging. Here $\boldsymbol{\mathcal{W}}_v$ and $\boldsymbol{\mathcal{W}}_c$ are mutually-uncorrelated white-noise random Gaussian tensor and vector fields with uncorrelated components,

$$\langle \mathcal{W}_{ij}^{(v)}(\mathbf{r}, t) \mathcal{W}_{kl}^{(v)}(\mathbf{r}', t') \rangle = (\delta_{ik} \delta_{jl}) \delta(t - t') \delta(\mathbf{r} - \mathbf{r}') \quad (6)$$

$$\langle \mathcal{W}_i^{(c)}(\mathbf{r}, t) \mathcal{W}_j^{(c)}(\mathbf{r}', t') \rangle = (\delta_{ij}) \delta(t - t') \delta(\mathbf{r} - \mathbf{r}'). \quad (7)$$

Similar covariance expressions apply in the Fourier domain as well if position \mathbf{r} (time t) is replaced by wavevector \mathbf{k} (wavefrequency ω), and $\langle \mathcal{W}_\alpha \mathcal{W}_\beta \rangle$ is replaced by $\langle \mathcal{W}_\alpha \mathcal{W}_\beta^* \rangle$, where star denotes complex conjugate (more generally, we denote an adjoint of a matrix or linear operator with a star).

We will assume that the viscosity and Soret coefficient are constants independent of the state, and that the product $\rho\chi = \rho_0\chi_0$ is constant as for a low-density gas, and that $c \ll 1$ so that $c(1-c) \approx c$. This allows us to write the viscous term in the momentum equation in the ‘‘Laplacian’’ form

$$\nabla \cdot [\eta \overline{\nabla} \mathbf{v} + \zeta (\nabla \cdot \mathbf{v}) \mathbf{I}] \rightarrow \eta \nabla^2 \mathbf{v} + \left(\zeta + \frac{\eta}{3} \right) \nabla (\nabla \cdot \mathbf{v}). \quad (8)$$

Similarly, the diffusive term in the concentration equation can be written as

$$\nabla \cdot [\rho\chi (\nabla c + c(1-c) S_T \nabla T)] \rightarrow \rho\chi [\nabla^2 c + S_T \nabla \cdot (c \nabla T)].$$

We will also neglect the concentration and temperature dependence of the equation of state and assume that $P = P(\rho) = P_0 + (\rho - \rho_0) c_T^2$, where c_T is a spatially-constant isothermal speed of sound.

If we further neglect density variations, $\rho = \rho_0 = \text{const.}$, we obtain the *incompressible* LLNS equations for a single-component fluid or a mixture of dynamically-identical fluids,

$$\partial_t \mathbf{v} = \mathcal{P} [-\mathbf{v} \cdot \nabla \mathbf{v} + \nu \nabla^2 \mathbf{v} + \rho^{-1} (\nabla \cdot \boldsymbol{\Sigma})] \quad (9)$$

$$= -\nabla \pi - \nabla \cdot (\mathbf{v} \mathbf{v}^T) + \nu \nabla^2 \mathbf{v} + \nabla \cdot \left(\sqrt{2\nu\rho^{-1}k_B T} \widetilde{\boldsymbol{\mathcal{W}}}_v \right)$$

$$\partial_t c = -\nabla \cdot [c(\mathbf{v} - \chi S_T \nabla T)] + \chi \nabla^2 c + \nabla \cdot \left[\sqrt{2\chi\rho^{-1}M c(1-c)} \boldsymbol{\mathcal{W}}_c \right], \quad (10)$$

where $\nu = \eta/\rho$, and $\mathbf{v} \cdot \nabla c = \nabla \cdot (c\mathbf{v})$ and $\mathbf{v} \cdot \nabla \mathbf{v} = \nabla \cdot (\mathbf{v}\mathbf{v}^T)$ because of incompressibility, $\nabla \cdot \mathbf{v} = 0$. Note that the velocity is not affected by the concentration in this incompressible approximation. Here \mathcal{P} is the orthogonal projection onto the space of divergence-free velocity fields, $\widehat{\mathcal{P}} = \mathbf{I} - k^{-2}(\mathbf{k}\mathbf{k}^*)$ in Fourier space (denoted with a hat) for periodic systems. Because of the projection of the stochastic forcing for incompressible flow, an equally-valid alternative is to replace the symmetric $\widetilde{\mathcal{W}}_{\mathbf{v}}$ above with the non-symmetric $\mathcal{W}_{\mathbf{v}}$, however, a strictly symmetric stochastic stress tensor ensures strict local conservation of angular momentum.

It is important to emphasize here that the non-linear LLNS equations, as written above, are ill-defined. These equations can be interpreted using a small-scale *regularization* (smoothing) of the stochastic forcing, along with a suitable renormalization of the transport coefficients [11, 51]. Such a regularization is naturally provided by the discretization length scale, and as long as there are sufficiently many molecules per hydrodynamic cell the fluctuations will be small and the behavior of the nonlinear equations will closely follow that of the *linearized* equations of fluctuating hydrodynamics, which can be given a precise meaning [52]. When analyzing and designing numerical schemes we focus on the linearized equations [28, 46], although the higher-order nonlinear effects are retained due to their physical significance [31].

Note that for the linearized equations there is no Ito-Stratonovich difficulty in interpreting the stochastic terms, and we therefore use the (ambiguous) ‘‘Langevin’’ notation that is standard in the physics literature, instead of the differential notation more common in the literature on stochastic differential equations. Some of the stochastic forcing terms considered here depend on the fluctuating fields themselves, for example, the covariance of Ψ in (22) is proportional to $c(1 - c)$, leading to additional nonlinearity and ambiguity in the equations. However, this dependence should be interpreted as being on the mean of the concentration \bar{c} , not including the (small) fluctuations around the mean, in the spirit of a linearization around the mean. That is, the stochastic forcing should not be considered multiplicative in the noise. However, since the mean is in general not known, we *estimate* it through local averages of a snapshot of the fluctuating fields.

A. Steady-State Covariances

The means and spatio-temporal covariances of the fluctuating fields fully characterize the Gaussian solution of the linearized equations [28]. Of particular importance is the steady-state covariance of the fluctuating fields, which can be obtained for periodic systems by linearizing the equations in the fluctuations and using a spatial Fourier transform to decouple the different modes (wavevectors \mathbf{k}). This steady-state covariance in Fourier space is usually referred to as a *static structure factor* in the physical literature, and represents the covariance matrix of the Fourier spectra of a typical snapshot of the fluctuating fields.

At thermodynamic equilibrium, the fluctuations of the different hydrodynamic variables are uncorrelated and white in space, that is, the equilibrium variance is independent of the wavevector \mathbf{k} [28], in agreement with equilibrium statistical mechanics [16, 53]. Consider first the isothermal compressible LLNS equations (1,2,3) linearized around a uniform steady-state, $(\rho, \mathbf{v}, c) = (\rho_0 + \delta\rho, \mathbf{v}_0 + \delta\mathbf{v}, c_0 + \delta c)$, $T = T_0$, along with the linearized equation of state

$$\delta P = P - P_0 = c_T^2 (\delta\rho),$$

where c_T is the isothermal speed of sound. Because of Galilean invariance, the advective terms $\mathbf{v}_0 \cdot \nabla(\square)$ due to the presence of a background flow do not affect the equilibrium covariances (structure factors), which are found to be [17, 28]

$$\begin{aligned} S_{\rho,\rho} &= \left\langle (\widehat{\delta\rho}) (\widehat{\delta\rho})^* \right\rangle = \rho_0 k_B T_0 / c_T^2 \\ \mathbf{S}_{\mathbf{v},\mathbf{v}} &= \left\langle (\widehat{\delta\mathbf{v}}) (\widehat{\delta\mathbf{v}})^* \right\rangle = \rho_0^{-1} k_B T_0 \mathbf{I} \\ S_{c,c} &= \left\langle (\widehat{\delta c}) (\widehat{\delta c})^* \right\rangle = M \rho_0^{-1} c_0 (1 - c_0). \end{aligned} \quad (11)$$

At equilibrium, there are no cross-correlations between the different variables, for example, $\mathbf{S}_{c,\mathbf{v}} = \left\langle (\widehat{\delta c}) (\widehat{\delta\mathbf{v}})^* \right\rangle = \mathbf{0}$. The equilibrium variance of the spatial average of a given variable over a cell of volume ΔV can be obtained by dividing the corresponding structure factor by ΔV , for example, the variance of the concentration is $\langle (\delta\rho)^2 \rangle = \rho_0 k_B T_0 / (c_T^2 \Delta V)$. In the incompressible limit, $c_T \rightarrow \infty$, the density fluctuations vanish and $\rho \approx \rho_0$.

Out of thermodynamic equilibrium, there may appear long-ranged correlations between the different hydrodynamic variables [17]. As a prototypical example of such non-equilibrium fluctuations, we focus on the incompressible equations (9,10) in the presence of an imposed concentration gradient $\nabla \bar{c}$. The spatial non-uniformity of the mean concentration when

there is a gradient breaks the translational symmetry and the Fourier transform no longer diagonalizes the equations. We focus our analysis and test our numerical schemes on a periodic approximation in which we linearize around a uniform background state $(\mathbf{v}, c) = (\delta\mathbf{v}, c_0 + \delta c)$ but mimic the effect of the advective term $\mathbf{v} \cdot \nabla c$ with an additional term $\mathbf{v} \cdot (\nabla \bar{c})$ in the concentration equation, to obtain the linearized equations in a periodic domain,

$$\begin{aligned}\partial_t(\delta\mathbf{v}) &= \mathcal{P} \left[\nu \nabla^2(\delta\mathbf{v}) + \nabla \cdot \left(\sqrt{2\nu\rho_0^{-1}k_B T_0} \mathcal{W}_v \right) \right] \\ \partial_t(\delta c) &= -(\nabla \bar{c}) \cdot (\delta\mathbf{v}) + \chi \nabla^2(\delta c) + \nabla \cdot \left[\sqrt{2\chi\rho_0^{-1}M c_0(1-c_0)} \mathcal{W}_c \right].\end{aligned}\quad (12)$$

In the Fourier domain (12) is a collection of stochastic differential equations, one system of linear additive-noise equations per wavevector \mathbf{k} , written in differential notation as

$$\begin{aligned}d(\widehat{\delta\mathbf{v}}) &= -\nu k^2 (\widehat{\delta\mathbf{v}}) dt + i\sqrt{2\nu\rho_0^{-1}k_B T_0} \widehat{\mathcal{P}} \mathbf{k} \cdot (d\mathcal{B}_v^{(\mathbf{k})}) \\ d(\widehat{\delta c}) &= -(\nabla \bar{c}) \cdot (\widehat{\delta\mathbf{v}}) dt - \chi k^2 (\widehat{\delta c}) dt + i\sqrt{2\chi\rho_0^{-1}M c_0(1-c_0)} \mathbf{k} \cdot (d\mathcal{B}_c^{(\mathbf{k})}),\end{aligned}\quad (13)$$

where we used that $\widehat{\mathcal{P}}(\widehat{\delta\mathbf{v}}) = \widehat{\delta\mathbf{v}}$. Here $\mathcal{B}_v(t)$ is a tensor, and $\mathcal{B}_c(t)$ is a vector, whose components are independent Wiener processes. Note that the velocity equation is not affected by the concentration gradient. Given the model equations (13), the explicit solution for the matrix of static structure factors (covariance matrix)

$$\mathcal{S} = \begin{bmatrix} \mathcal{S}_{v,v} & \mathcal{S}_{c,v}^* \\ \mathcal{S}_{c,v} & \mathcal{S}_{c,c} \end{bmatrix}$$

can be obtained as the solution of a linear system resulting from the stationarity condition $d\mathcal{S} = \mathbf{0}$ [28, 46].

1. Incompressible Velocity Fluctuations

By considering the stationarity condition $d\mathcal{S}_{v,v} = 0$ it can easily be seen that the equilibrium covariance of the velocities is proportional to the projection operator,

$$\mathcal{S}_{v,v} = \rho_0^{-1} k_B T_0 \widehat{\mathcal{P}} = \rho_0^{-1} k_B T_0 [\mathbf{I} - k^{-2}(\mathbf{k}\mathbf{k}^*)],\quad (14)$$

independent of the concentration gradient. In particular, the amplitude of the velocity fluctuations at each wavenumber is constant and reduced by one in comparison to the compressible equations,

$$\text{Tr } \mathcal{S}_{v,v} = \langle (\widehat{\delta\mathbf{v}})^* (\widehat{\delta\mathbf{v}}) \rangle = (d-1) \rho_0^{-1} k_B T_0,\quad (15)$$

where d is the spatial dimension. This is a reflection of the fact that one degree of freedom (i.e., one $k_B T/2$) is subtracted from the kinetic energy due to the incompressibility constraint, which eliminates the sound mode.

An alternative way of expressing the result (14) is that all divergence-free modes have the same power at equilibrium. That is, if the fluctuating velocities are expressed in any orthonormal basis for the space of velocities that satisfy $\nabla \cdot \mathbf{v} = 0$, at equilibrium the resulting random coefficients should be uncorrelated and have unit variance. This will be useful in Section IV A for examining the weak accuracy of the spatio-temporal discretizations of the incompressible equations. For periodic boundary conditions, such an orthonormal basis is simple to construct in the Fourier domain and a Fourier transform can be used project the velocity field onto this basis. In particular, for all wavevectors the projection of the velocity fluctuations onto the *longitudinal* mode

$$\hat{\mathbf{v}}^{(1)} = k^{-1} [k_x, k_y, k_z], \quad (16)$$

where $k = (k_x^2 + k_y^2 + k_z^2)^{1/2}$, should be identically zero,

$$\hat{v}_1 = (\widehat{\delta \mathbf{v}}) \cdot \hat{\mathbf{v}} = \frac{k_x}{k} \widehat{\delta v}_x + \frac{k_y}{k} \widehat{\delta v}_y + \frac{k_z}{k} \widehat{\delta v}_z = k^{-1} (\mathbf{k} \cdot \mathbf{v}) = 0.$$

A basis for the incompressible periodic velocity fields can be constructed from the two *vortical* modes

$$\hat{\mathbf{v}}^{(2)} = (k_x^2 + k_y^2)^{-1/2} [-k_y, k_x, 0], \quad (17)$$

$$\hat{\mathbf{v}}^{(3)} = k^{-1} (k_x^2 + k_y^2)^{-1/2} [k_x k_z, k_y k_z, - (k_x^2 + k_y^2)], \quad (18)$$

and the projection of the fluctuating velocities onto these modes has the equilibrium covariance

$$\langle \hat{v}_2 \hat{v}_2^* \rangle = \langle \hat{v}_3 \hat{v}_3^* \rangle = \rho_0^{-1} k_B T_0, \text{ while } \langle \hat{v}_2 \hat{v}_3^* \rangle = 0. \quad (19)$$

In two dimensions only $\hat{\mathbf{v}}^{(1)}$ and $\hat{\mathbf{v}}^{(2)}$ are present, and $\hat{\mathbf{v}}^{(2)}$ is the z component of the vorticity and spans the subspace of divergence-free velocities. The fact that the $(d-1)$ vortical modes have equal power leads to the velocity variance (15).

2. Nonequilibrium Fluctuations

When a macroscopic concentration gradient is present, the velocity fluctuations affect the concentration via the linearized advective term $(\nabla \bar{c}) \cdot \mathbf{v}$. Solving (13) shows an *enhancement*

of the concentration fluctuations [54] proportional to the square of the applied gradient,

$$S_{c,c} = M\rho_0^{-1} c_0(1 - c_0) + \frac{k_B T}{\rho\chi(\nu + \chi)k^4} (\sin^2 \theta) (\nabla\bar{c})^2, \quad (20)$$

where θ is the angle between \mathbf{k} and $\nabla\bar{c}$, $\sin^2 \theta = k_{\perp}^2/k^2$. Furthermore, there appear *long-range correlations* between the concentration fluctuations and the fluctuations of velocity parallel to the concentration gradient, proportional to the applied gradient [11, 54],

$$\mathcal{S}_{c,v_{\parallel}} = \left\langle (\widehat{\delta c})(\widehat{\delta v_{\parallel}}^*) \right\rangle = -\frac{k_B T}{\rho(\nu + \chi)k^2} (\sin^2 \theta) \nabla\bar{c}. \quad (21)$$

The power-law divergence for small k indicates long-range correlations between δc and $\delta \mathbf{v}$ and is the cause of the giant fluctuation phenomenon studied in Section V.

III. SPATIO-TEMPORAL DISCRETIZATION

Designing temporal discretizations for fluid dynamics is challenging even without including thermal fluctuations. When there is no stochastic forcing, our schemes revert to standard second-order discretizations and can be analyzed with existing numerical analysis techniques. Here we tackle the additional goal of constructing discretizations that, in a weak sense, accurately reproduce the statistics of the continuum fluctuations. The approach we follow is based on the ideas proposed in Ref. [28] and further elaborated in Ref. [46].

Thermal fluctuations are added to a deterministic scheme as an additional forcing term that represents the temporal average of a stochastic forcing term over the time interval Δt and over the spatial cells of volume ΔV [28]. Because \mathbf{W} is white in space and time, the averaging adds an additional prefactor of $(\Delta V \Delta t)^{-1/2}$ in front of the stochastic forcing. In the actual numerical schemes, a “realization” of a white-noise field \mathbf{W} is represented by a collection \mathbf{W} of normally-distributed random numbers with mean zero and covariance given by (7) or (6), with the identification

$$\mathbf{W} \longleftrightarrow (\Delta V \Delta t)^{-1/2} \mathbf{W}.$$

Specifically, the stochastic fluxes (4) are discretized as

$$\mathbf{\Sigma} = \sqrt{\frac{2\eta k_B T}{\Delta V \Delta t}} \mathbf{W}_v, \quad \text{and} \quad \mathbf{\Psi} = \sqrt{\frac{2\chi\rho M c(1-c)}{\Delta V \Delta t}} \mathbf{W}_c. \quad (22)$$

A realization of \mathbf{W} is sampled using a pseudo-random number stream. The temporal discretization of the stochastic forcing corresponds to the choice of how many realizations

of \mathbf{W} are generated per time step, and how each realization is associated to specific points in time inside a time step (e.g., the beginning, mid-point, or end-point of a time step). The spatial discretization corresponds to the choice of how many normal variates to generate per spatial cell, and how to associate them with elements of the spatial discretization (e.g., cell centers, nodes, faces, edges). Once these choices are made, it is simple to add the stochastic forcing to an existing deterministic algorithm or code, while still accounting for the fact that white-noise is not like a classical smooth forcing and cannot be evaluated pointwise.

A. Temporal Discretization

As a first step in designing a spatio-temporal discretization for the compressible and incompressible equations of fluctuating hydrodynamics, we focus on the temporal discretization. We assume that the time step is fixed at Δt . The time step index is denoted with a superscript, for example, \mathbf{c}^n denotes concentration at time $n\Delta t$ and \mathbf{W}^n denotes a realization of \mathbf{W} generated at time step n .

In the next section, we will describe our staggered spatial discretization of the crucial differential operators, denoted here rather generically with a letter symbol in order to distinguish them from the corresponding continuum operators. Specifically, let \mathbf{G} be the gradient (scalar \rightarrow vector), \mathbf{D} the divergence (vector \rightarrow scalar), and $\mathbf{L} = \mathbf{D}\mathbf{G}$ the Laplacian (scalar \rightarrow scalar) operator. When the divergence operator acts on a tensor field \mathbf{F} such as a stress tensor $\boldsymbol{\sigma}$, it is understood to act component-wise on the x , y and z components of the tensor. Similarly, the Laplacian acts component-wise on a vector. An important property of the discrete operators that we require to hold is that the divergence operator is the negative adjoint of the gradient, $\mathbf{D} = -\mathbf{G}^*$. This ensures that the scheme satisfies a discrete version of the continuous property,

$$\int_{\Omega} w [\nabla \cdot \mathbf{v}] d\mathbf{r} = - \int_{\Omega} \mathbf{v} \cdot \nabla w d\mathbf{r} \text{ if } \mathbf{v} \cdot \mathbf{n}_{\partial\Omega} = 0 \text{ or } \mathbf{v} \text{ is periodic}$$

for any scalar field $w(\mathbf{r})$.

We define the weak order of accuracy of a temporal discretization in terms of the mismatch between the steady-state covariance of the continuum and the discrete formulations. With periodic boundary conditions this would be the mismatch between the Fourier spectrum of a typical snapshot of the true solution and the steady-state discrete spectrum of the numerical

solution [28]. If this mismatch is $O(\Delta t^k)$, we say that the scheme has weak order of accuracy of $k \geq 1$, implying that for sufficiently small time steps the discrete formulation reproduces the steady-state covariance of the continuum formulation. A theoretical analysis of the weak accuracy of the temporal discretizations used in this work will be left for a future publication [46], here we simply state the main results and verify the order of weak accuracy numerically.

1. Compressible Equations

Denoting the fluctuating field with $\mathbf{Q} = (\rho, \mathbf{v}, c)$, the compressible LLNS equations (1,2,3) can be written as a general stochastic conservation law,

$$\partial_t \mathbf{Q} = -\mathbf{D} [\mathbf{F}(\mathbf{Q}; t) - \mathbf{Z}(\bar{\mathbf{Q}}, \mathbf{W})], \quad (23)$$

where \mathbf{D} is the divergence operator (acting component-wise on each flux), $\mathbf{F}(\mathbf{Q}; t)$ is the deterministic and $\mathbf{Z} = [0, \boldsymbol{\Sigma}, \boldsymbol{\Psi}]$ is the discretization of the stochastic flux (22). We recall that the stochastic forcing amplitude can in general depend on the unknown mean state, which we approximate with the instantaneous local (finite-volume) average, $\bar{\mathbf{Q}}(t) \approx \mathbf{Q}(t)$ in what follows. Following [29], we base our temporal discretization of (23) on the three-stage, low-storage total variation diminishing (TVD) Runge-Kutta (RK3) scheme of Gottlieb and Shu [55], ensuring stability in the inviscid limit without requiring slope-limiting. The stochastic terms are discretized using two random fluxes per time step, as proposed in Ref. [28]. This discretization achieves third-order weak accuracy [46] while only requiring the generation of two Gaussian random fields per time step.

For each stage of our third-order Runge-Kutta scheme, a conservative increment is calculated as

$$\Delta \mathbf{Q}(\mathbf{Q}, \mathbf{W}; t) = -\Delta t \mathbf{D} \mathbf{F}(\mathbf{Q}; t) + \Delta t \mathbf{D} \mathbf{Z}(\mathbf{Q}, \mathbf{W}).$$

Each time step of the RK3 algorithm is composed of three stages, the first one estimating \mathbf{Q} at time $t = (n + 1)\Delta t$, the second at $t = (n + \frac{1}{2})\Delta t$, and the final stage obtaining a third-order accurate estimate at $t = (n + 1)\Delta t$. Each stage consists of an Euler-Maryama

step followed by a weighted averaging with the value from the previous stage,

$$\begin{aligned}
\tilde{Q}^{n+1} &= Q^n + \Delta Q(Q^n, \mathbf{W}_1^n; n\Delta t) \\
\tilde{Q}^{n+\frac{1}{2}} &= \frac{3}{4}Q^n + \frac{1}{4}\left[\tilde{Q}^{n+1} + \Delta Q\left(\tilde{Q}^{n+1}, \mathbf{W}_2^n; (n+1)\Delta t\right)\right] \\
Q^{n+1} &= \frac{1}{3}Q^n + \frac{2}{3}\left[\tilde{Q}^{n+\frac{1}{2}} + \Delta Q\left(\tilde{Q}^{n+\frac{1}{2}}, \mathbf{W}_3^n; \left(n+\frac{1}{2}\right)\Delta t\right)\right],
\end{aligned} \tag{24}$$

where the stochastic fluxes between different stages are related to each other via

$$\begin{aligned}
\mathbf{W}_1^n &= \mathbf{W}_A^n - \sqrt{3}\mathbf{W}_B^n \\
\mathbf{W}_2^n &= \mathbf{W}_A^n + \sqrt{3}\mathbf{W}_B^n \\
\mathbf{W}_3^n &= \mathbf{W}_A^n,
\end{aligned} \tag{25}$$

and \mathbf{W}_A^n and \mathbf{W}_B^n are two independent realizations of \mathbf{W} that are generated independently at each RK3 step.

2. Incompressible Equations

The incompressible LLNS equations (9,10) can be written in the form

$$\begin{aligned}
\partial_t \mathbf{v} + \mathbf{G}\pi &= \mathbf{A}_v(\mathbf{v}, c) + \nu \mathbf{L}\mathbf{v} + \mathbf{D}[\Sigma(\bar{\mathbf{v}}, \bar{c}, \mathbf{W})], \\
\partial_t c &= \mathbf{A}_c(\mathbf{v}, c) + \chi \mathbf{L}c + \mathbf{D}[\Psi(\bar{\mathbf{v}}, \bar{c}, \mathbf{W})], \\
\text{s.t. } \mathbf{D}\mathbf{v}^* &= \mathbf{0},
\end{aligned}$$

where $\mathbf{A}(\mathbf{v}, c)$ represent the non-diffusive deterministic terms, such as the advective and Soret terms (with externally-imposed fixed temperature), as well as any additional terms arising from gravity or other effects. For generality, in the notation we allow for an arbitrary dependence of the stochastic forcing terms on the mean state, recalling that we approximate the mean state by the instantaneous local average of the fluctuating state, as for compressible flow.

We base our temporal discretization on the second-order semi-implicit deterministic scheme of Griffith [45]. Unlike a fractional-step scheme that splits the velocity and pressure updates [56, 57], this approach simultaneously solves for the velocity and pressure and avoids the need to determine appropriate ‘‘intermediate’’ boundary conditions. The ill-conditioning of the Stokes system is mitigated by using a projection method (an inhomogeneous Helmholtz

solve for velocity followed by a Poisson solve for the pressure) as a preconditioner. With periodic boundary conditions solving the Stokes system is equivalent to a projection method, that is, to an unconstrained step for the velocities followed by an application of the projection operator. Importantly, no spurious boundary modes [58, 59] arise due to the implicit velocity treatment even in the presence of physical boundaries, which is especially important for fluctuating hydrodynamics since all of the modes are stochastically forced [46].

The temporal discretization that we use is a predictor-corrector method in which the predictor step combines the Crank-Nicolson method for the diffusive terms with the Euler method for the remaining terms,

$$\begin{aligned} \frac{\tilde{\mathbf{v}}^{n+1} - \mathbf{v}^n}{\Delta t} + \mathbf{G}\tilde{\pi}^{n+\frac{1}{2}} &= \mathbf{A}_v(\mathbf{v}^n, c^n) + \nu \mathbf{L} \left(\frac{\tilde{\mathbf{v}}^{n+1} + \mathbf{v}^n}{2} \right) + \mathbf{D} [\boldsymbol{\Sigma}(\mathbf{v}^n, c^n, \mathbf{W}^n)], \\ \frac{\tilde{c}^{n+1} - c^n}{\Delta t} &= \mathbf{A}_c(\mathbf{v}^n, c^n) + \chi \mathbf{L} \left(\frac{\tilde{c}^{n+1} + c^n}{2} \right) + \mathbf{D} [\boldsymbol{\Psi}(\mathbf{v}^n, c^n, \mathbf{W}^n)] \\ \text{s.t. } \mathbf{D}\tilde{\mathbf{v}}^{n+1} &= \mathbf{0}. \end{aligned} \quad (26)$$

The corrector stage combines Crank-Nicolson for the diffusive terms with an explicit mid-point rule for the remaining deterministic terms, and uses the same realization of \mathbf{W} as in the predictor step,

$$\begin{aligned} \frac{\mathbf{v}^{n+1} - \mathbf{v}^n}{\Delta t} + \mathbf{G}\pi^{n+\frac{1}{2}} &= \mathbf{A}_v(\tilde{\mathbf{v}}^{n+\frac{1}{2}}, \tilde{c}^{n+\frac{1}{2}}) + \nu \mathbf{L} \left(\frac{\mathbf{v}^{n+1} + \mathbf{v}^n}{2} \right) + \mathbf{D} [\boldsymbol{\Sigma}(\tilde{\mathbf{v}}^{n+\frac{1}{2}}, \tilde{c}^{n+\frac{1}{2}}, \mathbf{W}^n)], \\ \frac{c^{n+1} - c^n}{\Delta t} &= \mathbf{A}_c(\tilde{\mathbf{v}}^{n+\frac{1}{2}}, \tilde{c}^{n+\frac{1}{2}}) + \chi \mathbf{L} \left(\frac{c^{n+1} + c^n}{2} \right) + \mathbf{D} [\boldsymbol{\Psi}(\tilde{\mathbf{v}}^{n+\frac{1}{2}}, \tilde{c}^{n+\frac{1}{2}}, \mathbf{W}^n)] \\ \text{s.t. } \mathbf{D}\mathbf{v}^{n+1} &= \mathbf{0}, \end{aligned} \quad (27)$$

where $\tilde{\mathbf{v}}^{n+\frac{1}{2}} = (\mathbf{v}^n + \tilde{\mathbf{v}}^{n+1})/2$ is a divergence free mid-point advection velocity, and $\tilde{c}^{n+\frac{1}{2}} = (c^n + \tilde{c}^{n+1})/2$. If advection were discretized semi-implicitly as well, that is, if $\mathbf{v}^{n+\frac{1}{2}} = (\mathbf{v}^n + \mathbf{v}^{n+1})/2$ were used when evaluating \mathbf{A}_v , the mid-point rule ensures strict kinetic energy conservation for inviscid flow.

In the case of a pure stochastic diffusion equation for the fluctuating fields, $\mathbf{A}(\mathbf{v}, c) = \mathbf{0}$, and stochastic fluxes that do not depend on the state, the corrector step is not necessary as it simply reproduces the predictor step. The resulting stochastic Crank-Nicolson method can be shown to have infinite order of weak accuracy, specifically, it can be shown that the correct steady-state covariance (but *not* the correct *dynamics*) is obtained for any time step size Δt [28, 46]. The Crank-Nicolson method therefore balances the numerical dissipation with the stochastic forcing identically. This unique property allows our time stepping to under-resolve

the fast dynamics of the small-wavelength fluctuations while still maintaining the correct spectrum for the fluctuations at all scales. When the advective terms are non-trivial, our temporal discretization is second-order in both the deterministic and the stochastic (weak) sense, while only requiring the generation of a single realization of the Gaussian random fields per time step.

Note that for the special case in which the momentum equation is independent of the concentration equation(s), it is possible to do the predictor/corrector stage for the velocity first, and then use the midpoint velocity $\mathbf{v}^{n+\frac{1}{2}}$ when calculating the advective terms in the concentration predictor/corrector stage. We employ this sort of *split* predictor-corrector method for the simulations of giant fluctuations reported in Section V.

B. Spatial Discretization

We now consider spatial discretization of the equations of fluctuating hydrodynamics on a regular Cartesian grid, focusing on two dimensions for notational simplicity. The spatial discretization is to be interpreted in the finite-volume sense, that is, the value of a fluctuating field at the center of a spatial cell of volume ΔV represents the average value of the fluctuating field over the cell. We explicitly enforce strict local conservation by using a conservative discretization of the divergence. Specifically, the change of the average value inside a cell can always be expressed as a sum of fluxes through each of the faces of the cell, even if we do not explicitly write it in that form.

Consider at first a simplified form of the stochastic advection-diffusion equation for a scalar concentration field

$$\partial_t c = \nabla \cdot \left[-c\mathbf{v} + \chi \nabla c + \sqrt{2\chi} \mathbf{W}_c \right], \quad (28)$$

where $\mathbf{v}(\mathbf{r}, t)$ is a given advection velocity. We note that for incompressible flow, if we split the stochastic stress tensor \mathbf{W}_v into a vector \mathbf{W}_x corresponding to the flux for \mathbf{v}_x , and a vector \mathbf{W}_y corresponding to \mathbf{v}_y , then the velocity equation becomes a constrained pair of stochastic advection-diffusion equations of the form (28). We will discuss the generalization to compressible flow in Section III B 5.

The spatial discretization described in this section is to be combined with a suitable stable temporal discretization, specifically, the temporal discretization that we employ was

described in Section III A. We consider here the limit of small time steps, $\Delta t \rightarrow 0$, corresponding formally to a semi-discrete “method of lines” spatial discretization of the form

$$\frac{d\mathbf{c}}{dt} = \mathbf{D} \left[(-\mathbf{U}\mathbf{c} + \chi\mathbf{G}\mathbf{c}) + \sqrt{2\chi/(\Delta V \Delta t)}\mathbf{W}_c \right], \quad (29)$$

where $\mathbf{c} = \{c_{i,j}\}$ is a finite-volume representation of the random field $c(\mathbf{r}, t)$. Here, \mathbf{D} is a conservative discrete divergence, \mathbf{G} is a discrete gradient, and $\mathbf{U} \equiv \mathbf{U}(\mathbf{v})$ denotes a discretization of advection by the spatially-discrete velocity field \mathbf{v} , and \mathbf{W}_c denotes a vector of uncorrelated normal variates with mean zero and unit variance.

1. Discrete Fluctuation-Dissipation Balance

We judge the weak accuracy of the spatial discretization by comparing the steady-state covariance of the spatially-discrete fields to the theoretical covariance of the continuum fields in the limit $\Delta t \rightarrow 0$ [28]. Ignoring for a moment constraints such as incompressibility, at thermodynamic equilibrium the variance of the discrete fields should be inversely proportional to ΔV and values in distinct cells should be uncorrelated

$$\mathbf{C}_c = \langle \mathbf{c}\mathbf{c}^* \rangle = S_{c,c} (\Delta V^{-1}\mathbf{I}). \quad (30)$$

For periodic systems this means that the spectral power of each discrete Fourier mode be equal to the continuum structure factor, $S_{c,c} = 1$ for the model equation (28) [see also (11)], independent of the wavenumber.

A spatial discretization that gives the correct equilibrium discrete covariance is said to satisfy the *discrete fluctuation-dissipation balance* (DFDB) condition [28, 46]. The condition guarantees that for sufficiently small time steps the statistics of the discrete fluctuations are consistent with the continuum formulation. For larger time steps, the difference between the discrete and continuum covariance will depend on the order of weak accuracy of the temporal discretization.

A simple way to obtain the DFDB condition is from the time stationarity of the covariance. For the model equation (28) we obtain the linear system of equations for the matrix \mathbf{C}_c ,

$$\frac{d\mathbf{C}_c}{dt} = \frac{d\langle \mathbf{c}\mathbf{c}^* \rangle}{dt} = \mathbf{D}(-\mathbf{U} + \chi\mathbf{G})\mathbf{C}_c + \mathbf{C}_c[\mathbf{D}(-\mathbf{U} + \chi\mathbf{G})]^* + 2\chi\Delta V^{-1}\mathbf{D}\mathbf{D}^* = \mathbf{0}, \quad (31)$$

whose solution we would like to be given by (30), specifically, $\mathbf{C}_c = \Delta V^{-1} \mathbf{I}$. Considering first the case of no advection, $\mathbf{U} = \mathbf{0}$, we obtain the requirement that $\mathbf{D}\mathbf{G} + (\mathbf{D}\mathbf{G})^* = -2\mathbf{D}\mathbf{D}^*$. A straightforward way to ensure this condition is to choose the discrete divergence and gradient operators to be negative adjoints of each other, $\mathbf{G} = -\mathbf{D}^*$, just as the continuum operators are [25, 28, 60]. As we will demonstrate numerically in Section IV, the staggered discretization of the dissipative and stochastic terms described below satisfies the discrete fluctuation-dissipation balance for both compressible and incompressible flow.

In the continuum equation (28), the advective term does not affect the fluctuation-dissipation balance at equilibrium; advection simply transports fluctuations without dissipating or amplifying them. This follows from the skew-adjoint property

$$\int_{\Omega} w [\nabla \cdot (c\mathbf{v})] d\mathbf{r} = - \int_{\Omega} c [\nabla \cdot (w\mathbf{v})] d\mathbf{r} \text{ if } \nabla \cdot \mathbf{v} = 0 \text{ and } \mathbf{v} \cdot \mathbf{n}_{\partial\Omega} = 0 \text{ or } \mathbf{v} \text{ is periodic,}$$

which holds for any scalar field $w(\mathbf{r})$. In particular, choosing $w \equiv c$ shows that for an advection equation $\partial_t c = -\nabla \cdot (c\mathbf{v})$ the “energy” $\int c^2 d\mathbf{r}/2$ is a conserved quantity. To ensure that the *discrete* fluctuation-dissipation balance (31) is satisfied, the matrix $\mathbf{D}\mathbf{U}\mathbf{C}_c$, or more precisely, the discrete advection operator $\mathbf{S} = \mathbf{D}\mathbf{U}$ should be skew-adjoint, $\mathbf{S}^* = -\mathbf{S}$. Specifically, denoting with $\mathbf{c} \cdot \mathbf{w} = \sum_{i,j} c_{i,j} w_{i,j}$ the discrete dot product, we require that for all \mathbf{w}

$$\mathbf{w} \cdot [(\mathbf{D}\mathbf{U}) \mathbf{c}] = -\mathbf{c} \cdot [(\mathbf{D}\mathbf{U}) \mathbf{w}] \quad (32)$$

if the advection velocities are discretely-divergence free, $(\mathbf{D}\mathbf{U}) \mathbf{1} = \mathbf{0}$, where $\mathbf{1}$ denotes a vector of all ones. Note that this last condition, $\mathbf{S}\mathbf{1} = \mathbf{0}$, ensures the desirable property that the advection is constant-preserving, that is, advection by the random velocities does not affect a constant concentration field.

For incompressible flow, the additional constraint on the velocity $\mathbf{D}\mathbf{v} = \mathbf{0}$ needs to be taken into account when considering discrete fluctuation-dissipation balance. In agreement with (14), we require that the equilibrium covariance of the discrete velocities be

$$\langle \mathbf{v}\mathbf{v}^* \rangle = \rho_0^{-1} k_B T_0 (\Delta V^{-1} \mathbb{P}), \quad (33)$$

where \mathbb{P} is the *discrete projection* operator

$$\mathbb{P} = \mathbf{I} - \mathbf{G} (\mathbf{D}\mathbf{G})^{-1} \mathbf{D} = \mathbf{I} - \mathbf{D}^* (\mathbf{D}\mathbf{D}^*)^{-1} \mathbf{D}.$$

With periodic boundary conditions, (33) implies that the discrete structure factor for velocity is $S_{\mathbf{v},\mathbf{v}} = \rho_0^{-1} k_B T_0 \widehat{\mathbb{P}}$. In particular, the variance of the velocity in each cell is in

agreement with the continuum result, since $\text{Tr } \widehat{\mathbb{P}} = \text{Tr } \widehat{\mathcal{P}} = d - 1$. More generally, for non-periodic or non-uniform systems, we require that for sufficiently small time steps all discretely-incompressible velocity modes are equally strong at equilibrium [46].

2. Staggered Grid

A cell-centered discretization that is of the form (29) and satisfies the discrete fluctuation-dissipation balance (DFDB) condition was developed for compressible flow in Ref. [28]. Extending this scheme to incompressible flow is, however, nontrivial. In particular, imposing a strict discrete divergence-free condition on collocated velocities has proven to be difficult and is often enforced only approximately [61], which is inconsistent with (33). An alternative is to use a staggered grid or ‘‘MAC’’ discretization, as first employed in projection algorithms for incompressible flow [62]. In this discretization, scalars are discretized at cell centers, i.e., placed at points (i, j) , while vectors (notably velocities) are discretized on faces of the grid, placing the x component at points $(i + 1/2, j)$, and the y component at $(i, j + 1/2)$. Such a staggered discretization is used for the fluxes in Ref. [28], the main difference here being that velocities are also staggered.

In the staggered discretization, the divergence operator maps from vectors to scalars in a locally-conservative manner,

$$\nabla \cdot \mathbf{v} \rightarrow (\mathbf{D}\mathbf{v})_{i,j} = \Delta x^{-1} \left(v_{i+\frac{1}{2},j}^{(x)} - v_{i-\frac{1}{2},j}^{(x)} \right) + \Delta y^{-1} \left(v_{i,j+\frac{1}{2}}^{(y)} - v_{i,j-\frac{1}{2}}^{(y)} \right).$$

The discrete gradient maps from scalars to vectors, for example, for the x component:

$$(\nabla c)_x \rightarrow (\mathbf{G}c)_{i+\frac{1}{2},j}^{(x)} = \Delta x^{-1} (c_{i+1,j} - c_{i,j}).$$

It is not hard to show that with periodic boundary conditions $\mathbf{G} = -\mathbf{D}^*$ as desired. The resulting Laplacian $\mathbf{L} = \mathbf{D}\mathbf{G}$ is the usual 5-point Laplacian,

$$\nabla^2 c \rightarrow (\mathbf{L}c)_{i,j} = \left[\Delta x^{-2} (c_{i-1,j} - 2c_{i,j} + c_{i+1,j}) + \Delta y^{-2} (c_{i,j-1} - 2c_{i,j} + c_{i,j+1}) \right],$$

which is positive definite except for the expected trivial translational zero modes. The velocities \mathbf{v}_x and \mathbf{v}_y can be handled analogously. For example, \mathbf{v}_x is represented on its own finite-volume grid, shifted from the concentration (scalar) grid by one half cell along the x axis. The divergence $\mathbf{D}^{(x)}$, gradient $\mathbf{G}^{(x)}$ and Laplacian $\mathbf{L}^{(x)}$ are the same MAC operators as for concentration, but shifted to the x -velocity grid.

For the compressible equations, there is an additional dissipative term in (8) that involves $\nabla(\nabla \cdot \mathbf{v})$. This term is discretized as written, $\mathbf{GD}\mathbf{v}$, which can alternatively be expressed in conservative form. When viscosity is spatially-dependent, the term $\nabla \cdot (\eta \overline{\nabla \mathbf{v}})$ should be discretized by calculating a viscous flux on each face of the staggered grids, interpolating viscosity as needed and using the obvious second-order centered differences for each of the terms $\partial_x v_x$, $\partial_x v_y$, $\partial_y v_y$ and $\partial_y v_x$. For a collocated velocity grid the mixed derivatives $\partial_x v_y$ and $\partial_y v_x$, and the corresponding stochastic forcing terms, do not have an obvious face-centered discretization and require a separate treatment [28].

3. Stochastic Fluxes

The stochastic flux \mathbf{W}_c , like other vectors, is represented on the faces of the grid, that is, \mathbf{W}_c is a vector of i.i.d. numbers, one number for each face of the grid. To calculate the state-dependent factor $\sqrt{c(1-c)}$ that appears in (22) on the faces of the grid, concentration is interpolated from the cell centers to the faces of the grid. At present, lacking any theoretical analysis, we use a simple arithmetic average (35) for this purpose.

The stochastic momentum flux \mathbf{W}_v is represented on the faces of the shifted velocity grids, which for a uniform grid corresponds to the *cell centers* (i, j) and the *nodes* $(i + \frac{1}{2}, j + \frac{1}{2})$ of the grid [20]. Two random numbers need to be generated for each cell center, $W_{i,j}^{(x)}$ and $W_{i,j}^{(y)}$, corresponding to the diagonal of the stochastic stress tensor. Two additional random numbers need to be generated for each node of the grid, $W_{i+\frac{1}{2},j+\frac{1}{2}}^{(x)}$ and $W_{i+\frac{1}{2},j+\frac{1}{2}}^{(y)}$, corresponding to the off-diagonal components. In three dimensions, the three diagonal components of the stochastic stress are represented at the cell centers, while the six off-diagonal components are represented at the *edges* of the grid, two random numbers per edge, for example, $W_{i+\frac{1}{2},j+\frac{1}{2},k}^{(x)}$ and $W_{i+\frac{1}{2},j+\frac{1}{2},k}^{(y)}$.

For the incompressible equations one can simply generate the different components of \mathbf{W}_v as uncorrelated normal variates with mean zero and unit variance, and obtain the correct equilibrium covariances. Alternatively, each realization of the stochastic stress can be made strictly symmetric and traceless as for compressible flow, as specified in (4). Because of the symmetry, in practice for each node or edge of the grid we generate only a single unit normal variate representing the two diagonally-symmetric components. For each cell center, we represent the diagonal components by generating d independent normal random numbers

of variance 2 and then subtracting their average from each number. Note that for collocated velocities a different approach is required because the diagonal and diagonally-symmetric components of the stress tensor are not discretized on the same grid [28].

4. Advection

We now consider skew-adjoint discretizations of the advection operator $\mathbf{S} = \mathbf{D}\mathbf{U}$ on a staggered grid. This problem has been considered in a more general context for the purpose of constructing stable methods for turbulent flow in Ref. [63, 64]; here we focus on a simple second-order centered discretization. The importance of the skew-adjoint condition in turbulent flow simulation is that it leads to strict discrete energy conservation for inviscid flow, which not only endows the schemes with long-time stability properties, but also removes undesirable numerical dissipation. Conservation of the discrete kinetic energy $E_k = \rho \langle \mathbf{v} \cdot \mathbf{v} \rangle / 2$ is also one of the crucial ingredients for fluctuation-dissipation balance, i.e., the requirement that the Gibbs-Boltzmann distribution $Z^{-1} \exp[-E_k / (k_B T)]$ be the invariant distribution of the stochastic velocity dynamics [19, 25, 65].

Consider first the spatial discretization of the advective term $\mathbf{D}\mathbf{U}\mathbf{c}$ in the concentration equation. Since divergence acts on vectors, which are represented on the faces of the grid, $\mathbf{U}\mathbf{c}$ should be represented on the faces as well, that is, \mathbf{U} is a linear operator that maps from cell centers to faces, and is a consistent discretization of the advective flux $\mathbf{c}\mathbf{v}$. If we define an advection velocity \mathbf{u} on the faces of the grid, and also define a concentration $\bar{\mathbf{c}}$ on each face of the grid, then the advective flux can directly be calculated on each face. For example, for the x faces:

$$(\mathbf{c}\mathbf{v})_x \rightarrow (\mathbf{U}\mathbf{c})_{i+\frac{1}{2},j}^{(x)} = u_{i+\frac{1}{2},j}^{(x)} c_{i+\frac{1}{2},j}. \quad (34)$$

For concentration we can take $\mathbf{u} = \mathbf{v}$, since the velocity is already represented on the faces of the scalar grid. Simple averaging can be used to interpolate scalars from cells to faces, for example,

$$c_{i+\frac{1}{2},j} = \frac{1}{2} (c_{i+1,j} + c_{i,j}), \quad (35)$$

although higher-order centered interpolations can also be used [28].

As discussed in Section III B 1, we require that the advection operator be skew adjoint if $\mathbf{D}\mathbf{U}\mathbf{1} = \mathbf{D}\mathbf{u} = \mathbf{0}$. Our temporal discretization of the incompressible equations (26,27)

ensures that a discretely divergence-free velocity is used for advecting all variables. The case of compressible flow will be discussed further in Section III B 5. In the incompressible case, $\mathbf{S} = \mathbf{DU}$ can be viewed as a second-order discretization of the “skew-symmetric” form of advection [63]

$$\mathbf{v} \cdot \nabla c + \frac{c}{2} \nabla \cdot \mathbf{v} = \frac{1}{2} [\nabla \cdot (c\mathbf{v}) + \mathbf{v} \cdot \nabla c].$$

Namely, using (34) we obtain

$$(\mathbf{DU}\mathbf{c})_{i,j} = \Delta x^{-1} \left(u_{i+\frac{1}{2},j}^{(x)} c_{i+\frac{1}{2},j} - u_{i-\frac{1}{2},j}^{(x)} c_{i-\frac{1}{2},j} \right) + \Delta y^{-1} \left(u_{i,j+\frac{1}{2}}^{(y)} c_{i,j+\frac{1}{2}} - u_{i,j-\frac{1}{2}}^{(y)} c_{i,j-\frac{1}{2}} \right),$$

and rewrite the x term using (35) as

$$\left(u_{i+\frac{1}{2},j}^{(x)} c_{i+\frac{1}{2},j} - u_{i-\frac{1}{2},j}^{(x)} c_{i-\frac{1}{2},j} \right) = \frac{1}{2} \left[\left(u_{i+\frac{1}{2},j}^{(x)} c_{i+1,j} - u_{i-\frac{1}{2},j}^{(x)} c_{i-1,j} \right) + c_{i,j} \left(u_{i+\frac{1}{2},j}^{(x)} - u_{i-\frac{1}{2},j}^{(x)} \right) \right],$$

and similarly for the y term, to obtain

$$(\mathbf{DU}\mathbf{c})_{i,j} = (\mathbf{S}\mathbf{c})_{i,j} = \left(\tilde{\mathbf{S}}\mathbf{c} \right)_{i,j} + \frac{1}{2} c_{i,j} (\mathbf{D}\mathbf{u})_{i,j}, \quad (36)$$

where $\tilde{\mathbf{S}}$ is a centered discretization of $[\nabla \cdot (c\mathbf{v}) + \mathbf{v} \cdot \nabla c]/2$,

$$\left(\tilde{\mathbf{S}}\mathbf{c} \right)_{i,j} = \frac{1}{2} \left[\Delta x^{-1} \left(u_{i+\frac{1}{2},j}^{(x)} c_{i+1,j} - u_{i-\frac{1}{2},j}^{(x)} c_{i-1,j} \right) + \Delta y^{-1} \left(u_{i,j+\frac{1}{2}}^{(y)} c_{i,j+1} - u_{i,j-\frac{1}{2}}^{(y)} c_{i,j-1} \right) \right]. \quad (37)$$

Since the advection velocity is discretely divergence free, $\mathbf{S} = \tilde{\mathbf{S}}$.

It is not hard to show that $\tilde{\mathbf{S}}$ is skew-adjoint. Consider the x term in $\left[\tilde{\mathbf{S}}\mathbf{c} \right] \cdot \mathbf{w}$, and, assuming periodic boundary conditions, shift the indexing from i to $i-1$ in the first sum and from i to $i+1$ in the second sum, to obtain

$$\sum_{i,j} w_{i,j} \left(u_{i+\frac{1}{2},j}^{(x)} c_{i+1,j} - u_{i-\frac{1}{2},j}^{(x)} c_{i-1,j} \right) = - \sum_{i,j} c_{i,j} \left(u_{i+\frac{1}{2},j}^{(x)} w_{i+1,j} - u_{i-\frac{1}{2},j}^{(x)} w_{i-1,j} \right).$$

Therefore, $\tilde{\mathbf{S}}$ is skew-adjoint, $\left(\tilde{\mathbf{S}}\mathbf{c} \right) \cdot \mathbf{w} = -\mathbf{c} \cdot \left(\tilde{\mathbf{S}}\mathbf{w} \right)$. A similar transformation can be performed with slip or stick boundary conditions as well. These calculations show that (32) holds and thus the discrete advection operator is skew-adjoint, as desired. Note that the additional terms in (10) due to the Soret effect can be included by advecting concentration with the effective velocity $\mathbf{v}_{\text{adv}} = \mathbf{v} - \chi S_T \nabla T$.

The same approach we outlined above for concentration can be used to advect the velocities as well. Each velocity component lives on its own staggered grid and advection velocities are needed on the faces of the shifted grid, which in two dimensions corresponds to the cell

centers and the nodes of the grid. The velocity \mathbf{v}_x is advected using an advection velocity field $\mathbf{u}^{(x)}$ that is obtained via a second-order interpolation of \mathbf{v} ,

$$\begin{aligned} (u_x^{(x)})_{i,j} &= \frac{1}{2} \left(v_{i-\frac{1}{2},j}^{(x)} + v_{i+\frac{1}{2},j}^{(x)} \right) \\ (u_y^{(x)})_{i+\frac{1}{2},j+\frac{1}{2}} &= \frac{1}{2} \left(v_{i,j+\frac{1}{2}}^{(y)} + v_{i+1,j+\frac{1}{2}}^{(y)} \right), \end{aligned}$$

and similarly for the other components. It is not hard to verify that the advection velocity $\mathbf{u}^{(x)}$ is discretely divergence-free if \mathbf{v} is:

$$\left(\mathbf{D}^{(x)} \mathbf{u}^{(x)} \right)_{i+\frac{1}{2},j} = \frac{1}{2} \left[(\mathbf{D}\mathbf{v})_{i,j} + (\mathbf{D}\mathbf{v})_{i+1,j} \right],$$

showing that $\mathbf{D}^{(x)} \mathbf{u}^{(x)} = \mathbf{0}$ if $\mathbf{D}\mathbf{v} = \mathbf{0}$. Therefore, the shifted advection operator $\mathbf{S}^{(x)} = \mathbf{D}^{(x)} \mathbf{U}^{(x)}$ is also skew-adjoint, as desired.

5. Compressible Equations

It is instructive at this point to summarize our spatial discretization of the incompressible equations (9,10), before turning to the compressible equations. The concentration equation (10) is discretized as

$$\frac{d\mathbf{c}}{dt} = -\mathbf{D}\mathbf{U}\mathbf{c} + \chi \mathbf{D}\mathbf{G}\mathbf{c} + \mathbf{D}\Psi, \quad (38)$$

where \mathbf{U} is given by (34) with advection velocity $\mathbf{u} = \mathbf{v} - \chi S_T \nabla T$. For the x component of the velocity we use the spatial discretization

$$\frac{d\mathbf{v}_x}{dt} + (\mathbf{G}\pi)_x = -\mathbf{D}^{(x)} \mathbf{U}^{(x)} \mathbf{v}_x + \eta \mathbf{D}^{(x)} \mathbf{G}^{(x)} \mathbf{v}_x + \rho^{-1} \mathbf{D}^{(x)} \Sigma^{(x)},$$

and similarly for the other components, and the pressure ensures that $\mathbf{D}\mathbf{v} = \mathbf{0}$.

Our staggered spatial discretization of the compressible equations (1,2,3) is closely based on the discretization described above for the incompressible equations. An important difference is that for compressible flow we use the conservative form of the equations, that is, we use the mass density ρ , the momentum density $\mathbf{j} = \rho\mathbf{v}$ and the partial mass density $\rho_1 = c\rho$ as variables. The momentum densities are staggered with respect to the mass densities. Staggered velocities are defined by interpolating density from the cell centers to the faces of the grid, for example,

$$\mathbf{v}_{i+\frac{1}{2},j}^{(x)} = \mathbf{j}_{i+\frac{1}{2},j}^{(x)} / \rho_{i+\frac{1}{2},j} = 2\mathbf{j}_{i+\frac{1}{2},j}^{(x)} / (\rho_{i+1,j} + \rho_{i,j}),$$

which implies that $\mathbf{D}\mathbf{j} = \mathbf{D}\mathbf{U}\boldsymbol{\rho}$.

The density equation (1) is discretized spatially as

$$\frac{d\boldsymbol{\rho}}{dt} = -\mathbf{D}\mathbf{U}\boldsymbol{\rho}, \quad (39)$$

while for the concentration equation (3) we use

$$\frac{d\rho_1}{dt} = -\mathbf{D}\mathbf{U}\rho_1 + \rho_0\chi_0\mathbf{D}\mathbf{G}\mathbf{c} + \mathbf{D}\boldsymbol{\Psi}, \quad (40)$$

where we assume that $\rho\chi = \rho_0\chi_0$ is constant. For the x component of the momentum density we use

$$\frac{d\mathbf{j}_x}{dt} = -\mathbf{D}^{(x)}\mathbf{U}^{(x)}\mathbf{j}_x - c_T^2(\mathbf{G}\boldsymbol{\rho})_x + \eta\mathbf{D}^{(x)}\mathbf{G}^{(x)}\mathbf{v}_x + \left(\zeta + \frac{\eta}{3}\right)(\mathbf{G}\mathbf{D}\mathbf{v})_x + \mathbf{D}^{(x)}\boldsymbol{\Sigma}^{(x)}, \quad (41)$$

and similarly for the other components. The spatio-temporal discretization ensures strict local conservation of ρ , \mathbf{j} and ρ_1 .

The discretization (39,40,41) satisfies discrete-fluctuation dissipation balance at equilibrium, specifically, the equilibrium covariances of velocity and density are $\langle\mathbf{v}\mathbf{v}^*\rangle = \rho_0^{-1}k_B T_0 \mathbf{I}$ and $\langle\rho\rho^*\rangle = \rho_0 k_B T_0 / c_T^2 \mathbf{I}$, in agreement with the continuum spectra given in (11). Linearizing the semi-discrete density equation (39) around an equilibrium state $(\boldsymbol{\rho}, \mathbf{v}) = (\boldsymbol{\rho}_0 + \delta\boldsymbol{\rho}, \mathbf{v}_0 + \delta\mathbf{v})$ with $\mathbf{D}\mathbf{v}_0 = \mathbf{0}$ gives

$$\frac{d(\delta\boldsymbol{\rho})}{dt} + \tilde{\mathbf{S}}_0(\delta\boldsymbol{\rho}) = -\rho_0[\mathbf{D}(\delta\mathbf{v})].$$

Recall that the operator $\tilde{\mathbf{S}}_0$, defined by (37) with $\mathbf{u} = \mathbf{v}_0$, is skew-adjoint, and the fluctuations in density are thus controlled by the coupling with the velocity fluctuations. For simplicity, consider this coupling for the case of a fluid at rest, $\mathbf{v}_0 = \mathbf{0}$ and thus $\delta\mathbf{j} = \rho_0(\delta\mathbf{v})$. Linearizing the momentum update (41) and focusing on the coupling with the density fluctuations, we obtain

$$\frac{d(\delta\mathbf{v})}{dt} + \text{advection} = -\rho_0^{-1}c_T^2[\mathbf{G}(\delta\boldsymbol{\rho})] + \text{dissipation and forcing}.$$

Fluctuation-dissipation balance requires the skew-symmetry property $\mathbf{L}_{\rho,\mathbf{v}}\langle\mathbf{v}\mathbf{v}^*\rangle = -\langle\rho\rho^*\rangle\mathbf{L}_{\mathbf{v},\rho}^*$, where $\mathbf{L}_{\rho,\mathbf{v}} = -\rho_0\mathbf{D}$ the operator in front of $\delta\mathbf{v}$ in the density equation, and $\mathbf{L}_{\mathbf{v},\rho} = -c_T^2\mathbf{G}$ is the operator in front of $\delta\boldsymbol{\rho}$ in the velocity equation. This skew-symmetry requirement is satisfied because of the key duality property $\mathbf{D} = -\mathbf{G}^*$. This demonstrates the importance of the duality between the discrete divergence and gradient operators, not just for a single advection-diffusion equation, but also for coupling between the different fluid variables.

6. Boundary Conditions

Non-periodic boundary conditions, specifically, Neumann or Dirichlet physical boundaries, can be incorporated into the spatial discretization by modifying the discrete divergence, gradient and Laplacian operators near a boundary. This needs to be done in a way that not only produces an accurate and robust deterministic scheme, but also ensures fluctuation-dissipation balance even in the presence of boundaries. Here we extend the approach first suggested in an Appendix in Ref. [13] to the staggered grid. It can be shown that the inclusion of the (discrete) incompressibility constraint does not affect the fluctuation-dissipation balance when an unsplit Stokes solver is employed in the temporal integrator [46].

We assume that the physical boundary is comprised of faces of the grid. Since only the direction perpendicular to the wall is affected, we focus on a one-dimensional system in which there is a physical boundary between cells 1 and 0. The fluctuation-dissipation condition requires that for each variable the covariance of the stochastic forcing \mathbf{DW} be equal to the negative discrete Laplacian operator \mathbf{L} ,

$$\mathbf{D} \langle \mathbf{W} \mathbf{W}^* \rangle \mathbf{D}^* = \mathbf{D} \mathbf{C}_w \mathbf{D}^* = -\mathbf{L}. \quad (42)$$

For the component of velocity perpendicular to the wall, some of the grid points are on the physical boundary itself and those values are held fixed and not included as independent degrees of freedom. For the second-order spatial discretization that we employ no values in cells outside of the physical domain are required. Therefore, no special handling at the boundary is needed.

For cell-centered quantities, such as concentration and components of the velocity parallel to the wall, the boundary is half a cell away from the cell center, that is, the boundary is staggered. In this case we use the same discrete operators near the boundaries as in the interior of the domain, using *ghost cells* extending beyond the boundaries to implement the finite-difference stencils near the boundaries. Consider first a Neumann condition on concentration, $\partial c(0)/\partial x = 0$. This means that a no-flux condition is imposed on the boundary, and therefore for consistency with physical conservation the stochastic flux on the boundary should also be set to zero, $W_{\frac{1}{2}} = 0$. The ghost cell value is set equal to the value in the neighboring interior cell (reflection), $c_0 = c_1$, leading to

$$(\mathbf{DW})_1 = \Delta x^{-1} W_{\frac{3}{2}}, \quad (\mathbf{Gc})_{\frac{1}{2}} = 0, \quad (\mathbf{Lc})_1 = \Delta x^{-1} (c_2 - c_1). \quad (43)$$

If we exclude points on the boundary from the domain of the divergence operator, which is also the range (image) of the gradient operator, then it is not hard to see that the duality condition $\mathbf{D}^* = -\mathbf{G}$ continues to hold. We can therefore continue to use uncorrelated unit normal variates for the stochastic fluxes not on the boundary, $\mathbf{C}_W = \mathbf{I}$ in (42).

If a Dirichlet condition $c(0) = 0$ is imposed, then the ghost cell value is obtained by a linear extrapolation of the value in the neighboring interior cell (inverse reflection), $c_0 = -c_1$, leading to

$$(\mathbf{D}\mathbf{W})_1 = \Delta x^{-1} \left(W_{\frac{3}{2}} - W_{\frac{1}{2}} \right), \quad (\mathbf{G}\mathbf{c})_{\frac{1}{2}} = \Delta x^{-1} (2c_1), \quad (\mathbf{L}\mathbf{c})_1 = \Delta x^{-1} (c_2 - 3c_1). \quad (44)$$

The duality condition $\mathbf{D}^* = -\mathbf{G}$ is no longer satisfied, but it is not hard to show that the fluctuation-dissipation balance condition (44) can be satisfied by simply doubling the variance of the stochastic flux on the boundary, $\langle W_{\frac{1}{2}} W_{\frac{1}{2}}^* \rangle = 2$. Note that the Laplacian (44) is not formally second-order accurate at the boundary, however, its normal modes (eigenvectors) can be shown to correspond exactly to the normal modes of the continuum Laplacian and have decay rates (eigenmodes) that are second-order accurate in Δx^2 , and in practice pointwise second-order accuracy is observed even next to the boundary. Formal second-order local accuracy can be obtained by using a quadratic extrapolation for the ghost cell, $c_0 = -2u_1 + u_2/3$ and $(\mathbf{L}\mathbf{c})_1 = \Delta x^{-1} (4c_2/3 - 4c_1)$, however, this requires a more complicated handling of the stochastic fluxes near the boundary as well.

In summary, the only change required to accommodate physical boundaries is to set the variance of stochastic fluxes on a physical boundary to zero (at Neumann boundaries), or to twice that used for the interior faces (at Dirichlet boundaries). For density in compressible flows, the ghost cell values are generated so that the pressure in the ghost cells is equal to the pressure in the neighboring interior cell, which ensures that there is no unphysical pressure gradient in the momentum equation across the interface. There is also no stochastic mass flux through faces on the boundary independent of the type of boundary condition at the wall.

IV. IMPLEMENTATION AND NUMERICAL TESTS

We now describe in more detail our implementations of the spatio-temporal discretizations described in Section III, and provide numerical evidence of their ability to reproduce the

correct fluctuation spectrum in uniform flows with periodic boundary conditions. A less trivial application with non-periodic boundaries is studied in Section V.

We consider here a uniform periodic system in which there is a steady background (mean) flow of velocity \mathbf{v}_0 . Unlike the continuum formulation, the discrete formulation is not Galilean-invariant under such uniform motion and the covariance of the discrete fluctuations is affected by the magnitude of \mathbf{v}_0 . The stability and accuracy of the spatio-temporal discretization is controlled by the dimensionless CFL numbers

$$\alpha = \frac{V\Delta t}{\Delta x}, \quad \beta = \frac{\nu\Delta t}{\Delta x^2}, \quad \text{and} \quad \beta_c = \frac{\chi\Delta t}{\Delta x^2},$$

where $V = c_T$ (isothermal speed of sound) for low Mach number compressible flow, and $V = \|\mathbf{v}_0\|_\infty$ for incompressible flow, and typically $\chi \ll \nu$. The explicit handling of the advective terms places a stability condition $\alpha \lesssim 1$, and the explicit handling of diffusion in the compressible flow case requires $\beta, \beta_c \leq 1/2^d$, where d is the dimensionality. The strength of advection relative to dissipation is measured by the cell Reynolds number $r = \alpha/\beta = V/(\nu\Delta x)$.

To characterize the weak accuracy of our methods we examine the discrete Fourier spectra of the fluctuating fields at equilibrium, and compare them to the continuum theory discussed in Section II A for all discrete wavenumbers \mathbf{k} . We use subscripts to denote which pair of variables is considered, and normalize each covariance so that for self-correlations we report the relative error in the variance, and for cross-correlations we report the correlation coefficient between the two variables. For example, the non-dimensionalized static structure factor for concentration is

$$\tilde{S}_{c,c} = \frac{\langle \hat{c}\hat{c}^* \rangle}{\Delta V^{-1} S_{c,c}} = \frac{\Delta V}{M\rho_0^{-1} c_0(1-c_0)} \langle \hat{c}\hat{c}^* \rangle,$$

where $\hat{c}(\mathbf{k})$ is the discrete Fourier transform of the concentration. Note that an additional factor equal to the total number of cells may be needed in the numerator depending on the exact definition used for the discrete Fourier transform [28]. Similarly, the cross-correlations between different variables need to be examined as well, such as for example,

$$\tilde{S}_{c,v} = \frac{\Delta V}{\sqrt{[M\rho_0^{-1} c_0(1-c_0)] (\rho_0^{-1} k_B T_0)}} \langle \hat{c}\hat{\mathbf{v}}^* \rangle.$$

For staggered variables the shift between the corresponding grids should be taken into account as a phase shift in Fourier space, for example, $\exp(k_x\Delta x/2)$ for v_x . For a perfect

scheme, $\tilde{S}_{c,c} = 1$ and $\tilde{\mathbf{S}}_{c,v} = \mathbf{0}$ for all wavenumbers, and discrete fluctuation-dissipation balance in our discretization ensures this in the limit $\Delta t \rightarrow 0$. Our goal will be to quantify the deviations from “perfect” for several methods, as a function of the dimensionless numbers α and β .

A. Incompressible Solver

We have implemented the incompressible scheme described in Sections III A 2 and III B using the IBAMR software framework [66], an open-source library for developing fluid-structure interaction models that use the immersed boundary method. The IBAMR framework uses SAMRAI [67] to manage Cartesian grids in parallel, and it uses PETSc [68] to provide iterative Krylov solvers. The majority of the computational effort in the incompressible solver is spent in the linear solver for the Stokes system; in particular, in the projection-based preconditioner, the application of which requires solving a linear Poisson system for the pressure, and a modified linear Helmholtz system for the velocities and the concentrations [45]. For small viscous CFL numbers $\beta \ll 1$ the Poisson solver dominates the cost, however, for $\beta \gg 1$ the two linear systems become similarly ill-conditioned and require a good preconditioner themselves. We employ the *hypre* library [69] to solve the linear systems efficiently using geometric multigrid solvers. Note that with periodic boundary conditions the velocity and the pressure linear systems decouple and Fast Fourier Transforms could be used to solve them efficiently.

For incompressible flow, one could directly compare the spectrum of the velocities $\langle \hat{\mathbf{v}} \hat{\mathbf{v}}^* \rangle$ to the spectrum of the discrete projection operator \mathbb{P} (see Section III B 1). It is, however, simpler and more general to instead examine the equilibrium covariance of the discrete modes forming an orthonormal basis for the space of discretely divergence free modes. The amplitude of each mode should be unity for all wavenumbers, even if there are physical boundaries present, making it easy to judge the accuracy at different wavenumbers. For periodic boundary conditions a discretely-orthogonal basis is obtained by replacing the wavenumber $\mathbf{k} = (k_x, k_y, k_z)$ in (16,17,18) by the effective wavenumber $\tilde{\mathbf{k}}$ that takes into account the centered discretization of the projection operator, for example,

$$\tilde{k}_x = \frac{\exp(ik_x\Delta x/2) - \exp(-ik_x\Delta x/2)}{i\Delta x} = k_x \frac{\sin(k_x\Delta x/2)}{(k_x\Delta x/2)}. \quad (45)$$

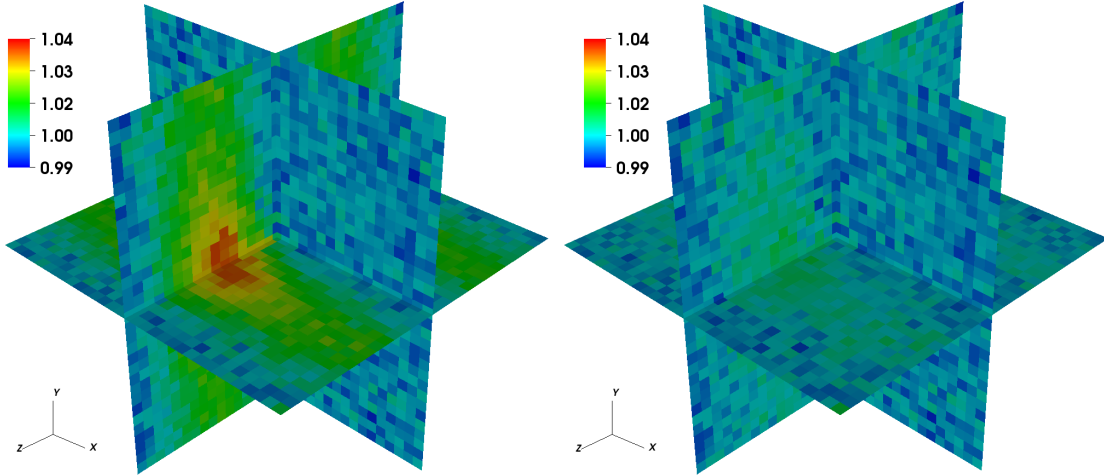


Figure 2: Spectral power of the first solenoidal mode for an incompressible fluid, $\tilde{S}_{\mathbf{v}}^{(2)}(k_x, k_y, k_z)$, as a function of the wavenumber (ranging from 0 to $\pi/\Delta x$ along each axes), for a periodic system with 32^3 cells. A uniform background flow along the z axis is imposed. The left panel is for a time step $\alpha = 0.5$, and the right for $\alpha = 0.25$. Though not shown, we find that $\tilde{S}_{\mathbf{v}}^{(3)}$ and $\tilde{S}_{c,c}$ are essentially identical, and both the real and imaginary parts of the cross-correlation $\tilde{S}_{\mathbf{v}}^{(2,3)}$ vanish to within statistical accuracy.

Our temporal discretization ensures that the discrete velocities are discretely divergence free, that is, $\langle \hat{v}_1 \hat{v}_1^* \rangle = 0$ to within the tolerance of the linear solvers used for the Stokes system. For a perfect scheme, the dimensionless structure factor

$$\tilde{S}_{\mathbf{v}}^{(2)} = \frac{\Delta V}{\rho_0^{-1} k_B T_0} \langle \hat{v}_2 \hat{v}_2^* \rangle,$$

and analogously $\tilde{S}_{\mathbf{v}}^{(3)}$ (in three dimensions) would be unity for all wavenumbers, while $\tilde{S}_{\mathbf{v}}^{(2,3)} \sim \langle \hat{v}_2 \hat{v}_3^* \rangle$ would be zero.

Note that for a system at equilibrium, $\nabla \bar{c} = \mathbf{0}$, the linearized velocity equation and the concentration equation (12) are uncoupled and thus $\tilde{\mathbf{S}}_{c,v} = \mathbf{0}$. Observe that the same temporal discretization is used for the velocity equation, projected onto the space of discretely divergence-free vector fields consistent with the boundary conditions, and for the concentration equation. Therefore, it is sufficient to present here numerical results for only one of the self-correlations $\tilde{S}_{\mathbf{v}}^{(2)}$, $\tilde{S}_{\mathbf{v}}^{(3)}$ and $\tilde{S}_{c,c}$. In Fig. 2 we show $\tilde{S}_{\mathbf{v}}^{(2)}$ as a function of the wavenumber \mathbf{k} in three dimensions for a cell Reynolds number $r = 1$ and an advective CFL number $\alpha = 0.5$ and $\alpha = 0.25$. Even for the relatively large time step, the deviation from unity is less than

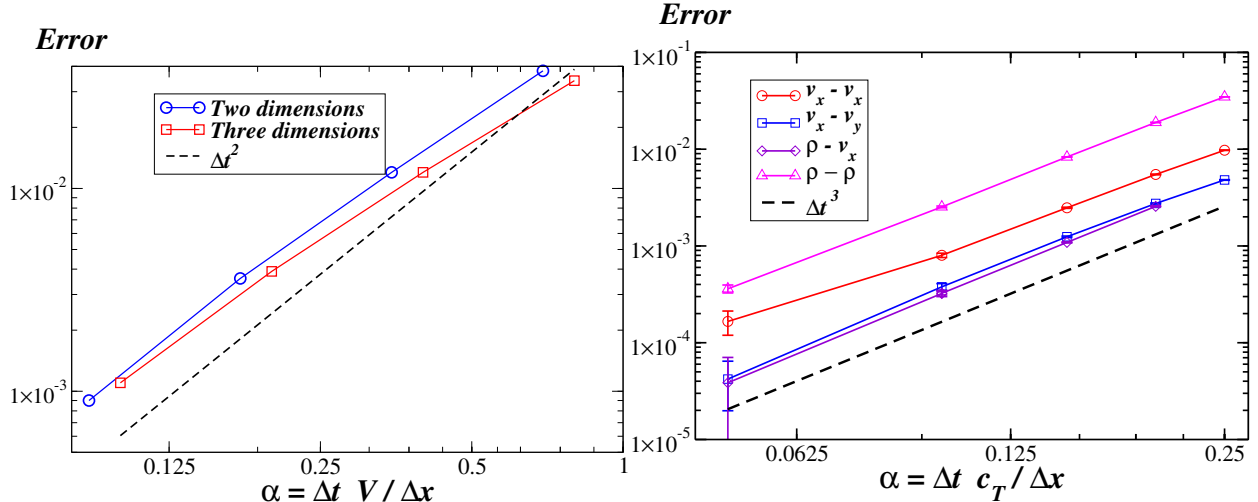


Figure 3: (Left) Relative error in the equilibrium variance of velocity (or, equivalently, concentration) for several time steps, as obtained using our incompressible code with a background flow velocity $\mathbf{v}_0 = (\sqrt{3}, 2)/2$ corresponding to cell Reynolds number $r = \sqrt{3}/2$ in two dimensions, and $\mathbf{v}_0 = (1, 1/3, 1/3)$ corresponding to $r = 1$ in three dimensions, for a grid of size 32^2 and 32^3 cells, respectively. The theoretical order of convergence $O(\Delta t^2)$ is shown for comparison. Error bars are on the order of the symbol size. (Right) Normalized covariance of the discrete velocities and densities compared to the theoretical expectations, using the parameters reported in the caption of Fig. 4. The value reported is the relative error of the variance of a variable or the correlation coefficient between pairs of variables, see legend. The theoretical order of convergence $O(\Delta t^3)$ is shown for comparison. Error bars are indicated but are smaller than the symbol size except for the smallest time step.

5%, and as $\alpha \rightarrow 0$ it can be shown theoretically and observed numerically that the correct covariance is obtained at all wavenumbers.

Theoretical analysis suggests that the error in the discrete covariance vanishes with time step and the background velocity as $O(\alpha^2) \sim O(V^2 \Delta t^2)$ for both velocity and concentration [46]. In the left panel of Fig. 3 we show the observed relative error in the variance of the discrete velocity as a function of α , confirming the predicted quadratic convergence. As expected, identical results are obtained for concentration as well. These numerical results confirm that our spatial discretization satisfies discrete fluctuation-dissipation balance and the temporal discretization is weakly second-order accurate.

B. Compressible Solver

Unlike the incompressible method, which requires complex linear solvers and preconditioners, the explicit compressible scheme is very simple and easy to parallelize on Graphics Processing Units (GPUs). Our implementation is written in the CUDA programming environment, and is three-dimensional with the special case of $N_z = 1$ cell along the z axes corresponding to a quasi two-dimensional system. In our implementation we create one thread per cell, and each thread only writes to the memory address associated with its cell and only accesses the memory associated with its own and neighboring cells. This avoids concurrent writes and costly synchronizations between threads, facilitating efficient execution on the GPU. Further efficiency is gained by using the GPU texture unit to perform some of the simple computations such as evaluating the equation of state. Our GPU code running in a NVIDIA GeForce GTX 480 is about 4 times faster (using double precision) than a compressible CPU-based code [28] running on 32 AMD cores using MPI.

We first examine the equilibrium discrete Fourier spectra of the density and velocity fluctuations for a uniform periodic system with an imposed background flow, with similar results observed for concentration fluctuations. In Fig. 4 we show the correlations of density and velocity fluctuations as a function of the wavenumber \mathbf{k} in three dimensions for a CFL number of $\alpha = 0.25$. We see that self-correlations are close to unity while cross-correlations nearly vanish, as required, with density fluctuations having the largest relative error of 5% for the largest wavenumbers.

Calculating cross-correlations in real space is complicated by the staggering of the different grids. We arbitrarily associate one half of the cell faces with the cell center, defining $\langle(\delta\rho)(\delta v_x)\rangle \equiv \left\langle(\delta\rho_{i,j})\left(\delta v_{i+\frac{1}{2},j}^{(x)}\right)\right\rangle$ and $\langle(\delta v_x)(\delta v_y)\rangle \equiv \left\langle\left(\delta v_{i+\frac{1}{2},j}^{(x)}\right)\left(\delta v_{i,j+\frac{1}{2}}^{(y)}\right)\right\rangle$. Theoretical analysis suggests that the error in the discrete covariance vanishes with time step as $O(\alpha^3) \sim O(c_T^3 \Delta t^3)$ [46]. In the right panel of Fig. 3 we show the relative error in the discrete covariances as a function of α in the presence of a background flow, confirming the predicted cubic convergence. These numerical results verify that our spatial discretization satisfies discrete fluctuation-dissipation balance and the temporal discretization is weakly third-order accurate.

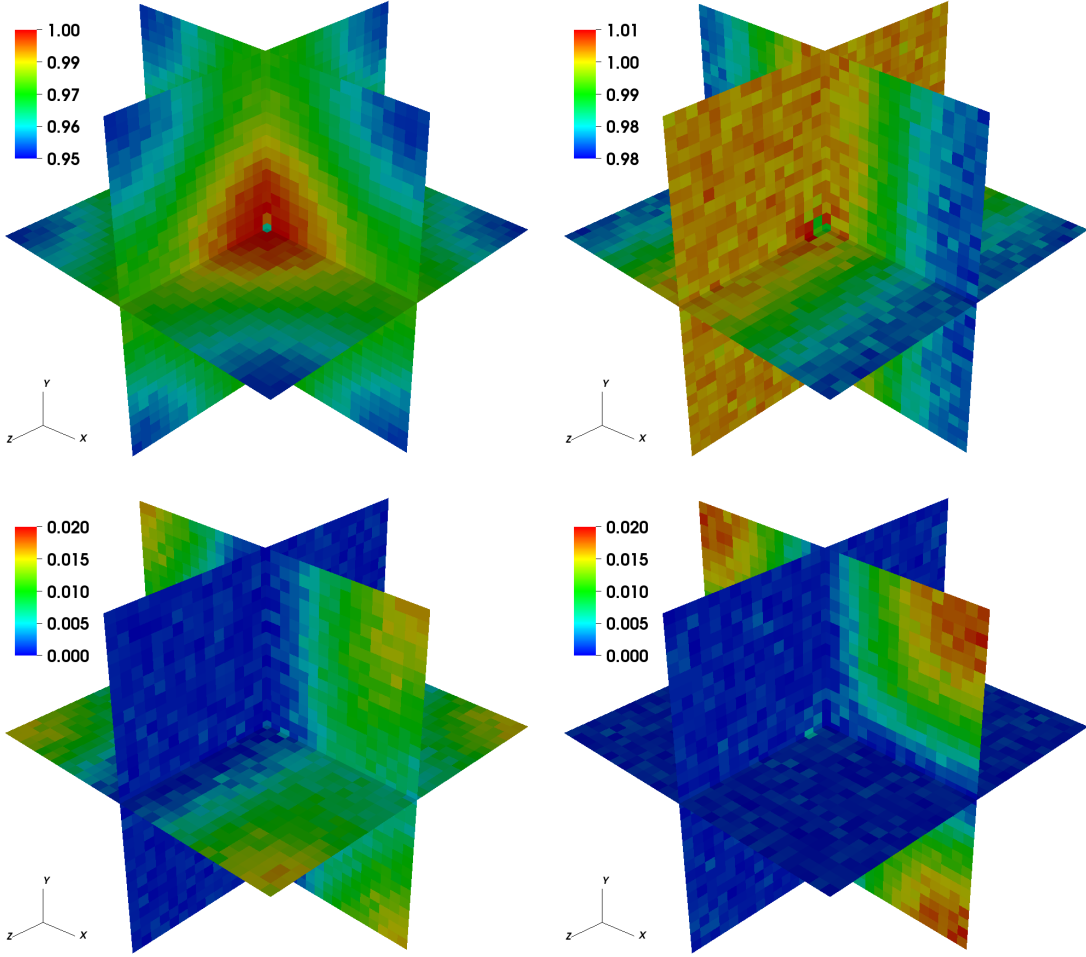


Figure 4: Normalized static structure factors $\tilde{S}_{\rho,\rho}$ (top left), \tilde{S}_{v_x,v_x} (top right), \tilde{S}_{ρ,v_x} (bottom left) and \tilde{S}_{v_x,v_y} (bottom right) for a compressible fluid with physical properties similar to water, for a periodic system with 30^3 cells. A uniform background flow with velocity $v_0 = (0.2, 0.1, 0.05)c_T$ is imposed and the time step corresponds to an acoustic CFL number $\alpha = 0.25$ and viscous CFL number $\beta_\nu = 0.017$ for shear viscosity and $\beta_\zeta = 0.041$ for bulk viscosity.

1. Dynamic Correlations

For compressible flow, the dynamics of the fluctuations is affected by the presence of sound waves and it is important to verify that the numerical scheme is able to reproduce the temporal correlations between the fluctuations of the different pairs of variables. In particular, a good method should reproduce the dynamic correlations at small wavenumbers and wave-frequencies correctly [28]. Theoretical predictions for the equilibrium covariances of

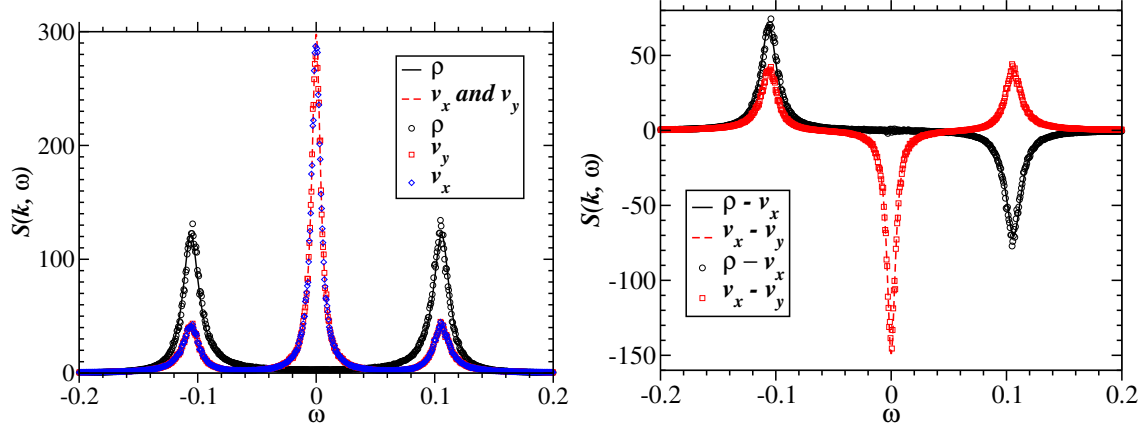


Figure 5: Numerical data (symbols) and theory (lines) for the real part of several dynamic structure factors for wavenumber $\mathbf{k} = (2, 2, 2) \cdot 2\pi/L$ in a cubic periodic box of 30^3 cells and volume L^3 . Self correlations are shown in the left panel, and cross-correlations are shown in the right panel. The imaginary part vanishes to within statistical accuracy for the off-diagonal terms. The physical parameters are as reported in the caption of Fig. 4.

the spatio-temporal spectra of the fluctuating fields, usually referred to as *dynamic structure factors*, are easily obtained by solving the equations (1,2) in the Fourier wavevector-frequency (\mathbf{k}, ω) domain and averaging over the fluctuations of the stochastic forcing [17]. The density-density dynamic structure factor $S_{\rho,\rho}(\mathbf{k}, \omega)$ is accessible experimentally via light scattering measurements, and for isothermal flow it exhibits two symmetric Brillouin peaks at $\omega \approx \pm c_T k$. The velocity components exhibit an additional central Rayleigh peak at $\omega = 0$ due to the viscous dissipation. As the fluid becomes less compressible (i.e., the speed of sound increases), there is an increasing separation of time-scales between the side and central spectral peaks, showing the familiar numerical stiffness of the compressible Navier-Stokes equations.

In Fig. 5 we compare the theoretical to the numerical dynamic structure factors for one of the smallest resolved wavenumbers, and observe very good agreement. Note that unlike static correlations, dynamic correlations are subject to discretization artifacts for larger wavenumbers, even as $\Delta t \rightarrow 0$ [28]. Specifically, the positions and widths of the various peaks are set by the effective wavevector $\tilde{\mathbf{k}}$ rather than the true wavevector \mathbf{k} , as given for the standard second-order discretization of diffusion in (45).

V. GIANT FLUCTUATIONS

As a non-trivial application of our staggered schemes for fluctuating hydrodynamics, we perform the first incompressible computer simulations of diffusive mixing in microgravity, recently studied experimentally aboard a satellite in orbit around the Earth [12]. The experimental data presented in Ref. [12] shows good agreement with theoretical predictions, however, various over-simplifications are made in the theory, notably, only the solenoidal velocity mode with the largest wavelength is considered. Numerical simulations allow for a more detailed comparison of experimental data with fluctuating hydrodynamics.

The experimental configuration consists of a dilute solution of polystyrene in toluene, confined between two parallel transparent plates that are a distance $h = 1\text{mm}$ apart. A steady temperature gradient $\nabla\bar{T} = \Delta T/h$ is imposed along the y axes via the plates. The weak temperature gradient leads to a strong concentration gradient $\nabla\bar{c} = \bar{c}S_T(\nabla\bar{T})$ due to the Soret effect, giving rise to an exponential steady-state concentration profile $\bar{c}(y)$. Quantitative shadowgraphy is used to observe and measure the strength of the fluctuations in the concentration around \bar{c} via the change in the refraction index. The observed light intensity, once corrected for the optical transfer function of the equipment, is proportional to the intensity of the fluctuations in the concentration averaged along the gradient,

$$c_{\perp}(x, z) = h^{-1} \int_{y=0}^h c(x, y, z) dy.$$

Additional details of the experimental setup and parameters are given in Ref. [12].

If temperature fluctuations are neglected, $T = \bar{T}(y)$, the incompressible equations (9,10) can be used to model the experimental setup. In our simulations, the plates are represented by no-slip boundaries at $y = 0$ and $y = h$, and periodic boundaries are imposed along the x and z axis to mimic the large extents of the system in the directions perpendicular to the gradient. A Robin boundary condition is used for concentration at the physical boundary,

$$\frac{\partial c}{\partial n} = -cS_T(\mathbf{n} \cdot \nabla\bar{T}),$$

ensuring that the normal component of the concentration flux vanishes at a physical boundary. The stochastic concentration flux also vanishes at the boundary as for Dirichlet boundaries, since the Soret term does not affect fluctuation-dissipation balance. In the codes the

boundary condition is imposed by setting the concentration in a ghost cell to

$$c_g = c_n \frac{2 \pm S_T (\nabla \bar{T}) \Delta y}{2 \mp S_T (\nabla \bar{T}) \Delta y},$$

where c_n is the value in the neighboring cell in the interior of the computational domain, and the sign depends on whether the ghost cell is at the low or high end of the y axes. The boundary condition is imposed explicitly, which leads to non-conservation of the total concentration when a semi-implicit method is used for the diffusive terms in the concentration equation. This can be corrected by implementing the boundary condition implicitly or using an explicit method for concentration; however, we do not do either since the observed change in the average concentration is small for the specific parameters we use.

For large wavenumbers the influence of the boundaries can be neglected and the periodic theory presented in Section II A 1 applied. Numerically, this sort of quasi-periodic model is implemented by using periodic boundary conditions but adding an additional source term $-\mathbf{v} \cdot \nabla \bar{c}$ in the concentration equation, as in (12). This term mimics our skew-adjoint discretization of the advection by the fluctuating velocities

$$\mathbf{v} \cdot \nabla \bar{c} \rightarrow (\mathbf{D}U\bar{c})_{i,j} = \frac{\nabla \bar{c}}{2} \left(v_{i,j+\frac{1}{2}}^{(y)} + v_{i,j-\frac{1}{2}}^{(y)} \right),$$

and is conservative when integrated over the whole domain. Note that in this quasi-periodic setup $\nabla \bar{c}$ is simply an externally-imposed quantity unrelated to the actual mean concentration profile.

By definition of the three-dimensional Fourier transform, the spectrum of the fluctuations of c_\perp can be obtained from the full three-dimensional spectrum (20) by setting $k_y = k_\parallel = 0$. For the specific parameters in question the equilibrium fluctuations in concentration are negligible even at the largest resolved wavenumbers. When discretization artifacts are taken into account, the quasi-periodic theoretical prediction for the experimentally-observed spectrum becomes

$$S_{\text{QP}}^\perp(k_x, k_z) = \left\langle \left(\widehat{\delta c_\perp} \right) \left(\widehat{\delta c_\perp} \right)^* \right\rangle = \frac{k_B T}{\rho [\chi(\nu + \chi)] \tilde{k}_\perp^4} (\nabla \bar{c})^2, \quad (46)$$

where $\tilde{k}_\perp^4 = \left(\tilde{k}_x^2 + \tilde{k}_z^2 \right)^2$ and tilde denotes the effective wavenumber (45). Imposing no-slip conditions for the fluctuating velocities makes the theory substantially more complicated. A single-mode approximation for the velocities is made in Ref. [70] in order to obtain a closed-form expression for the spectrum of concentration fluctuations in a non-periodic system S_{NP}^\perp .

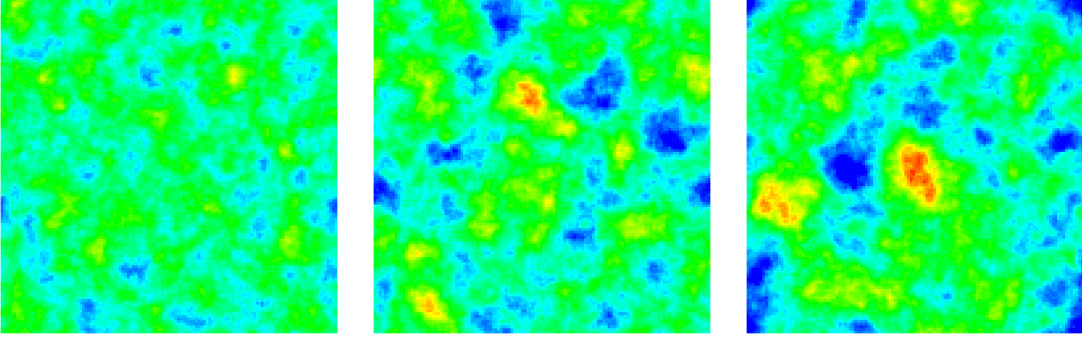


Figure 6: Snapshots of the concentration c_{\perp} in the plane perpendicular to the gradient $\nabla\bar{c}$, at times $0.1\tau_0$, τ_0 , and $5\tau_0$ after the gradient is established. The thickness of the sample (perpendicular to the page) is one quarter of the lateral extents of the system, $h = L_y = L_x/4$, and sets the scale of the steady-state fluctuations. Compare to the experimental snapshots shown in Fig. 1 of Ref. [12].

For a small Lewis number and without gravity it is found that

$$\frac{S_{\text{NP}}^{\perp}(\mathbf{k}_{\perp})}{S_{\text{QP}}^{\perp}(\mathbf{k}_{\perp})} \approx G(hk_{\perp}) = \frac{q_{\perp}^4}{q_{\perp}^4 + 24.6q_{\perp}^2 + 500.5}, \quad (47)$$

where $q_{\perp} = hk_{\perp}$ is a non-dimensionalized wavenumber. In reality the concentration profile is exponential rather than linear, and we take the effective concentration gradient to be $\nabla\bar{c} \approx \Delta c/h$, where Δc is the difference in concentration near the two boundaries.

The Galerkin function G given by (47) reflects the physical intuition that the no-slip condition suppresses fluctuations at scales larger than the distance between the physical boundaries [12]. After the concentration gradient is established, “giant” [41] concentration fluctuations evolve with a typical time scale of $\tau_0 = h^2/(\pi^2\chi) \sim 1000\text{s}$, until a steady state is reached in which the typical length scale of the concentration fluctuations is set by the finite extent of the domain. This is illustrated in Fig. 6 via snapshots of $c_{\perp}(x, z; t)$ taken at several points in time after starting with no concentration fluctuations at time $t = 0$.

The large speed of sound in toluene makes the compressible equations very stiff at the length scales of the experimental system. It is usually argued that compressibility does not affect the concentration fluctuations [17]. Solving the compressible equations in the presence of a concentration gradient confirms that, as long as there is a large separation of time scales between the acoustic and diffusive dynamics, the presence of sound waves does not affect the concentration fluctuations. In our compressible simulations, we artificially decrease the speed of sound many-fold and set the cell Reynolds number to $r = c_T/(\nu\Delta x) = 10$.

Numerical results show that this is sufficient to approach the limit $r \rightarrow \infty$ to within the statistical accuracy of our results. This decrease in c_T corresponds to making the mass of the toluene molecules much larger than the mass of the polystyrene macromolecules themselves, which is of course physically very unrealistic. One can think of our compressible simulations of giant fluctuations in microgravity as an artificial compressibility method for solving the incompressible equations. The true incompressible simulations allow for a much larger time step, not only because of the lack of acoustics, but also because of the implicit temporal discretization of the viscous terms in the momentum equations. However, it is important to remember that a time step of our GPU-parallelized compressible code takes much less computing than a time step of the incompressible code. Nevertheless, we are able to study larger system sizes in three dimensions using the incompressible algorithm.

In the actual experiments reported in Ref. [12], concentration diffusion is much slower than momentum diffusion, corresponding to Schmidt number $\nu/\chi = s \approx 3 \cdot 10^3$. This level of stiffness makes direct simulation of the temporal dynamics of the fluctuations infeasible, as long averaging is needed to obtain accurate steady-state spectra, especially for small wavenumbers. However, as far as the static correlations are concerned, we see from (46) that the crucial quantity is $\chi(\nu + \chi) = (s + 1)\chi^2$, rather than χ and ν individually. Therefore, we can artificially increase χ and decrease ν to reduce s , keeping $s \gg 1$ and $(s + 1)\chi^2$ fixed. It can be proven more formally that there exists a limiting stochastic process for the concentration as $s \rightarrow \infty$ so long as $s\chi^2$ is kept constant (E. Vanden-Eijnden, private communication).

In Fig. 7 we show numerical results for the steady-state spectrum of the discrete concentration field averaged along the y -axes, in two (left panel) and in three dimensions (right panel), for both bulk (quasi-periodic) and finite (non-periodic) systems. In order to compare with the theoretical predictions (46) and (47) most directly, we plot the ratio of the observed to the predicted spectrum. This choice of normalization not only emphasizes any mismatch with the theory, but also eliminates the power-law (k_{\perp}^{-4}) divergence and makes it easier to average over nearby wavenumbers \tilde{k}_{\perp} and also estimate error bars¹. For the runs reported in Fig. 7 we applied the largest concentration (temperature) gradient ($\Delta T = 17.4\text{K}$) used

¹ Note, however, that the most reliable error bars are obtained by averaging over many *uncorrelated* runs started with different random number seeds.

in the experiments [12]; we have verified that the non-equilibrium concentration fluctuations scale as the square of the gradient.

Both panels in Fig. 7 show an excellent agreement between the theory (46) and the numerical results for quasi-periodic systems. This shows that correcting for the spatial discretization artifacts by replacing k_{\perp} with \tilde{k}_{\perp} accounts for most of the discretization error. For the compressible runs, we use a relatively small time step, $\alpha = 0.2$, leading to temporal discretization errors that are smaller than the statistical accuracy except at the largest wavenumbers. The majority of the incompressible simulations employ a time step corresponding to a viscous CFL number $\beta = 1$ or $\beta = 2$, but we obtain identical results for larger β as well. It can be shown that our semi-implicit discretization of the incompressible equations gives the correct static covariance of the concentration for *all* time step sizes, as long as a mid-point estimate of the velocity is used when computing advective fluxes for concentration [46]. This is true even though the advective terms are handled explicitly because the concentration does not affect the velocity, that is, there is no buoyancy force due to gravity. To avoid a redundant predictor step for the velocity equation we use a split time stepping scheme in which velocity is advanced first and then the midpoint estimate for velocity is used to advect concentration in both the predictor and corrector steps.

In the left panel of Fig. 7 we compare results from two-dimensional compressible and incompressible simulations and find excellent agreement. For non-periodic systems the single-mode Galerkin theory (47) is not exact and the theory visibly over-predicts the concentration fluctuations for smaller wavenumbers in both two and three dimensions. We observe only a partial overlap of the data for different Schmidt numbers $s = \nu/\chi$ for smaller wavenumbers, although the difference between $s = 10$ and $s = 20$ is relatively small.

In three dimensions, we rely on the incompressible code in order to reach time scales necessary to obtain sufficiently accurate steady-state averages for large Schmidt numbers. In the right panel of Fig. 7 we compare numerical results for quasi-periodic and non-periodic compressible and incompressible systems to the theoretical predictions and also to experimental data from Ref. [12] (A. Vailati, private communication). The experimental data has substantial measurement uncertainties, and is presently normalized by an arbitrary pre-factor. Within this arbitrary normalization, our numerical results seem to be in good agreement with the experimental observations over the whole range of experimentally-accessible wavenumbers, and the agreement at small wavenumbers improves as the Schmidt number of

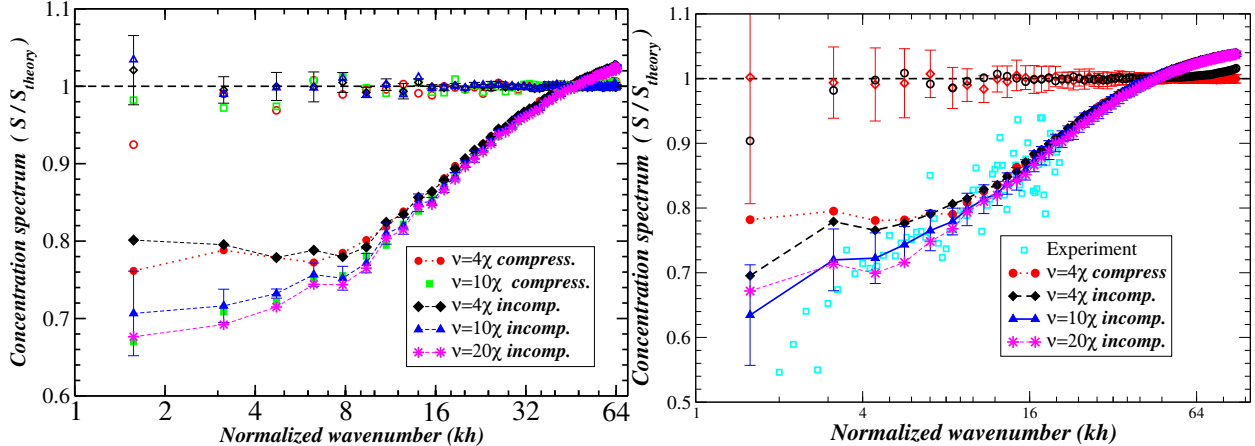


Figure 7: Ratio between the numerical and theoretical discrete spectrum of concentration projected along the y axes, as a function of the normalized wavenumber $q_{\perp} = k_{\perp}h$. For all runs $N_y = 32$ cubic hydrodynamic cells along the y axes were used, and all systems have aspect ratio $N_x/N_y = N_z/N_y = 4$. Error bars are indicated for some of the curves to indicate the typical level of statistical uncertainty. (Left) Two dimensions, for both compressible and incompressible fluids (see legend), with either periodic boundary conditions (empty symbols) or physical boundaries (solid symbols) imposed at the y -boundaries, for several Schmidt numbers $s = \nu/\chi$. (Right) Three dimensions, with same symbols as left panel), along with arbitrarily normalized experimental data [12] (see legend) corresponding to $s \approx 3 \cdot 10^3$ (courtesy of A. Vailati).

the simulations increases. The actual magnitude of the *macroscopic* non-equilibrium fluctuations in c_{\perp} is given by the integral of the structure factor $S_{c,c}^{\perp}$ over all wavenumbers \mathbf{k}_{\perp} . Numerically we observe fluctuations $\langle (\delta c_{\perp})^2 \rangle / \bar{c}_{\perp}^2 \approx 3 \cdot 10^{-7}$, which is consistent with experimental estimates (A. Vailati, private communication).

VI. CONCLUSIONS

We have presented spatio-temporal discretizations of the equations of fluctuating hydrodynamics for both compressible and incompressible mixtures of dynamically-identical isothermal fluids. As proposed by some of us in Ref. [28], we judge the weak accuracy of the schemes by their ability to reproduce the equilibrium covariances of the fluctuating variables. In particular, for small time steps the spatial discretization ensures that each mode is equally forced and dissipated in agreement with the fluctuation-dissipation balance principle satis-

fied by the continuum equations. A crucial ingredient of this discrete fluctuation-dissipation balance is the use of a discrete Laplacian $\mathbf{L} = -\mathbf{D}\mathbf{D}^*$ for the dissipative fluxes, where \mathbf{D} is a conservative discrete divergence, with a suitable correction to both the Laplacian stencil and the stochastic fluxes at physical boundaries. Furthermore, we utilize a centered skew-adjoint discretization of advection which does not additionally dissipate or force the fluctuations, as previously employed in long-time simulations of turbulent flow, where it is also crucial to ensure conservation and avoid artificial dissipation [63].

For the compressible equations, our spatio-temporal discretization is closely based on the collocated scheme proposed by some of us in Ref. [28], except that here we employ a staggered velocity grid. It is important to point that out the difference between a *collocated* scheme, in which the fluid variables are cell-centered but the stochastic fluxes are face-centered (staggered), as described in Ref. [28], and a *centered* scheme where *all* quantities are cell-centered. Several authors [26, 27] have already noted that centered schemes lead to a Laplacian that decouples neighboring cells, which is problematic in the context of fluctuating hydrodynamics. We emphasize however that these problems are not shared by collocated schemes for compressible fluids, for which the Laplacian $\mathbf{L} = -\mathbf{D}\mathbf{D}^*$ has the usual compact $2d + 1$ stencil, where d is the dimensionality [28]. Discretizations in which all conserved quantities are collocated may be preferred over staggered ones in particle-continuum hybrids [13], or more generally, in conservative discretizations for non-uniform grids.

A staggered grid arrangement, however, has a distinct advantage for incompressible flow. Namely, the use of a staggered grid simplifies the construction of a robust idempotent discrete projection $\mathbb{P} = \mathbf{I} + \mathbf{D}^*\mathbf{L}^{-1}\mathbf{D}$ that maintains discrete fluctuation-dissipation at all wavenumbers. In the temporal discretization employed here, based on prior work by one of us [45], this projection is used as a preconditioner for solving the Stokes equations for the pressure and velocities at the next time step. For periodic systems the method becomes equivalent to a classical Crank-Nicolson-based projection method, while at the same time avoiding the appearance of artificial pressure modes in the presence of physical boundaries [58, 59].

The numerical results presented in Section V verify that our numerical simulations model experimental measurements of giant fluctuations [12] during diffusive mixing of fluids faithfully. The numerical simulations give access to a lot more data than experimentally measurable. For example, the spectrum of concentration fluctuations in the $x - z$ plane can be

computed for planes (slices) as the distance from the boundaries is varied, giving a more complete picture of the three dimensional spatial correlations of the nonequilibrium fluctuations. We defer a more detailed analysis, including a study of temporal correlations, to future work.

The compressible solver we developed utilizes modern GPUs for accelerating the computations. In the future we will investigate the use of GPUs for the incompressible equations, starting with simple FFT-based solvers for periodic systems. For grid sizes that are much larger than molecular scales, the stability restriction of explicit compressible solvers becomes severe and it becomes necessary to eliminate sound waves from the equations by employing the low Mach number limit. A challenge that remains to be addressed in future work is the design of zero Mach number methods [71] for solving the variable-density equations of fluctuating hydrodynamics, as necessary when modeling mixtures of miscible fluids with different densities. This would enable computational modeling of the effects of buoyancy (gravity) in experimental studies of the giant fluctuation phenomenon performed on Earth [38, 41, 42].

Acknowledgments

We thank Alberto Vailati for insightful comments and sharing experimental data from the GRADFLEX experiments [12]. We thank Alejandro Garcia for a careful reading and suggestions on improving this work. We thank Eric Vanden-Eijnden for inspiring discussions. B. Griffith acknowledges research support from the National Science Foundation under awards OCI 1047734 and DMS 1016554. J. Bell and A. Donev were supported by the DOE Applied Mathematics Program of the DOE Office of Advanced Scientific Computing Research under the U.S. Department of Energy under contract No. DE-AC02-05CH11231. Additional support for A. Donev was provided by the National Science Foundation under grant DMS-1115341. R. Delgado-Buscalioni and F. Balboa acknowledge funding from the Spanish government FIS2010-22047-C0S and from the Comunidad de Madrid MODELICO-CM

(S2009/ESP-1691).

- [1] L. Bocquet and E. Charlaix. Nanofluidics, from bulk to interfaces. *Chemical Society Reviews*, 39(3):1073–1095, 2010.
- [2] L. Wang and M. Quintard. Nanofluids of the future. *Advances in Transport Phenomena*, pages 179–243, 2009.
- [3] A. Naji, P. J. Atzberger, and Frank L. H. Brown. Hybrid elastic and discrete-particle approach to biomembrane dynamics with application to the mobility of curved integral membrane proteins. *Phys. Rev. Lett.*, 102(13):138102, 2009.
- [4] C.S. Peskin, G.M. Odell, and G.F. Oster. Cellular motions and thermal fluctuations: the Brownian ratchet. *Biophysical Journal*, 65(1):316–324, 1993.
- [5] E. Frey and K. Kroy. Brownian motion: a paradigm of soft matter and biological physics. *Annalen der Physik*, 14(1-3):20–50, 2005.
- [6] R. Delgado-Buscalioni, E. Chacon, and P. Tarazona. Hydrodynamics of nanoscopic capillary waves. *Phys. Rev. Lett.*, 101(10):106102, 2008.
- [7] B. Z. Shang, N. K. Voulgarakis, and J.-W. Chu. Fluctuating hydrodynamics for multiscale simulation of inhomogeneous fluids: Mapping all-atom molecular dynamics to capillary waves. *J. Chem. Phys.*, 135:044111, 2011.
- [8] M. Moseler and U. Landman. Formation, stability, and breakup of nanojets. *Science*, 289(5482):1165–1169, 2000.
- [9] B. Davidovitch, E. Moro, and H.A. Stone. Spreading of viscous fluid drops on a solid substrate assisted by thermal fluctuations. *Phys. Rev. Letters*, 95(24):244505, 2005.
- [10] Y. Hennequin, D. G. A. L. Aarts, J. H. van der Wiel, G. Wegdam, J. Eggers, H. N. W. Lekkerkerker, and D. Bonn. Drop formation by thermal fluctuations at an ultralow surface tension. *Phys. Rev. Lett.*, 97(24):244502, 2006.
- [11] A. Donev, A. L. Garcia, Anton de la Fuente, and J. B. Bell. Diffusive Transport Enhanced by Thermal Velocity Fluctuations. *Phys. Rev. Lett.*, 106(20):204501, 2011.
- [12] A. Vailati, R. Cerbino, S. Mazzoni, C. J. Takacs, D. S. Cannell, and M. Giglio. Fractal fronts of diffusion in microgravity. *Nature Communications*, 2:290, 2011.
- [13] A. Donev, J. B. Bell, A. L. Garcia, and B. J. Alder. A hybrid particle-continuum method for

- hydrodynamics of complex fluids. *SIAM J. Multiscale Modeling and Simulation*, 8(3):871–911, 2010.
- [14] C. W. Gardiner. *Handbook of stochastic methods: for physics, chemistry & the natural sciences*, volume Vol. 13 of *Series in synergetics*. Springer, third edition, 2003.
- [15] N. G. van Kampen. *Stochastic Processes in Physics and Chemistry*. Elsevier, third edition, 2007.
- [16] L.D. Landau and E.M. Lifshitz. *Fluid Mechanics*, volume 6 of *Course of Theoretical Physics*. Pergamon Press, Oxford, England, 1959.
- [17] J. M. O. De Zarate and J. V. Sengers. *Hydrodynamic fluctuations in fluids and fluid mixtures*. Elsevier Science Ltd, 2006.
- [18] A.L. Garcia, M. Malek Mansour, G. Lie, and E. Clementi. Numerical integration of the fluctuating hydrodynamic equations. *J. Stat. Phys.*, 47:209, 1987.
- [19] B. Dunweg and A.J.C. Ladd. Lattice Boltzmann simulations of soft matter systems. *Adv. Comp. Sim. for Soft Matter Sciences III*, pages 89–166, 2009.
- [20] N. Sharma and N. A. Patankar. Direct numerical simulation of the Brownian motion of particles by using fluctuating hydrodynamic equations. *J. Comput. Phys.*, 201:466–486, 2004.
- [21] G. De Fabritiis, M. Serrano, R. Delgado-Buscalioni, and P. V. Coveney. Fluctuating hydrodynamic modeling of fluids at the nanoscale. *Phys. Rev. E*, 75(2):026307, 2007.
- [22] G. Giupponi, G. De Fabritiis, and P. V. Coveney. Hybrid method coupling fluctuating hydrodynamics and molecular dynamics for the simulation of macromolecules. *J. Chem. Phys.*, 126(15):154903, 2007.
- [23] R. Delgado-Buscalioni and G. De Fabritiis. Embedding molecular dynamics within fluctuating hydrodynamics in multiscale simulations of liquids. *Phys. Rev. E*, 76(3):036709, 2007.
- [24] P. J. Atzberger, P. R. Kramer, and C. S. Peskin. A stochastic immersed boundary method for fluid-structure dynamics at microscopic length scales. *J. Comput. Phys.*, 224:1255–1292, 2007.
- [25] P. J. Atzberger. Stochastic Eulerian-Lagrangian Methods for Fluid-Structure Interactions with Thermal Fluctuations. *J. Comp. Phys.*, 230:2821–2837, 2011.
- [26] N. K. Voulgarakis and J.-W. Chu. Bridging fluctuating hydrodynamics and molecular dynamics simulations of fluids. *J. Chem. Phys.*, 130(13):134111, 2009.
- [27] R. Delgado-Buscalioni and A. Dejoan. Nonreflecting boundaries for ultrasound in fluctuating

- hydrodynamics of open systems. *Phys. Rev. E*, 78(4):046708, 2008.
- [28] A. Donev, E. Vanden-Eijnden, A. L. Garcia, and J. B. Bell. On the Accuracy of Explicit Finite-Volume Schemes for Fluctuating Hydrodynamics. *CAMCOS*, 5(2):149–197, 2010.
- [29] J.B. Bell, A.L. Garcia, and S.A. Williams. Numerical methods for the stochastic Landau-Lifshitz Navier-Stokes equations. *Phys. Rev. E*, 76:016708, 2007.
- [30] J.B. Bell, A. Garcia, and S. Williams. Computational fluctuating fluid dynamics. *ESAIM: M2AN*, 44(5):1085–1105, 2010.
- [31] A. Donev, A. L. Garcia, Anton de la Fuente, and J. B. Bell. Enhancement of Diffusive Transport by Nonequilibrium Thermal Fluctuations. *J. of Statistical Mechanics: Theory and Experiment*, 2011:P06014, 2011.
- [32] S.V. Patankar. *Numerical heat transfer and fluid flow*. Hemisphere Pub, 1980.
- [33] B.E. Griffith. A Comparison of Two Adaptive Versions of the Immersed Boundary Method. 2010.
- [34] A. L. Garcia, M. Malek Mansour, G. C. Lie, M. Mareschal, and E. Clementi. Hydrodynamic fluctuations in a dilute gas under shear. *Phys. Rev. A*, 36(9):4348–4355, 1987.
- [35] M. Mareschal, M.M. Mansour, G. Sonnino, and E. Kestemont. Dynamic structure factor in a nonequilibrium fluid: A molecular-dynamics approach. *Phys. Rev. A*, 45:7180–7183, May 1992.
- [36] J. R. Dorfman, T. R. Kirkpatrick, and J. V. Sengers. Generic long-range correlations in molecular fluids. *Annual Review of Physical Chemistry*, 45(1):213–239, 1994.
- [37] J.M. Ortiz de Zarate and J.V. Sengers. On the physical origin of long-ranged fluctuations in fluids in thermal nonequilibrium states. *J. Stat. Phys.*, 115:1341–59, 2004.
- [38] A. Vailati and M. Giglio. Nonequilibrium fluctuations in time-dependent diffusion processes. *Phys. Rev. E*, 58(4):4361–4371, 1998.
- [39] C. J. Takacs, G. Nikolaenko, and D. S. Cannell. Dynamics of long-wavelength fluctuations in a fluid layer heated from above. *Phys. Rev. Lett.*, 100(23):234502, 2008.
- [40] D. Brogioli. Giant fluctuations in diffusion in freely-suspended liquid films. *ArXiv e-prints*, 2011.
- [41] A. Vailati and M. Giglio. Giant fluctuations in a free diffusion process. *Nature*, 390(6657):262–265, 1997.
- [42] D. Brogioli, A. Vailati, and M. Giglio. Universal behavior of nonequilibrium fluctuations in

- free diffusion processes. *Phys. Rev. E*, 61(1):1–4, 2000.
- [43] A. Vailati, R. Cerbino, S. Mazzoni, M. Giglio, G. Nikolaenko, C.J. Takacs, D.S. Cannell, W.V. Meyer, and A.E. Smart. Gradient-driven fluctuations experiment: fluid fluctuations in microgravity. *Applied Optics*, 45(10):2155–2165, 2006.
- [44] F. Croccolo, D. Brogioli, A. Vailati, M. Giglio, and D. S. Cannell. Nondiffusive decay of gradient-driven fluctuations in a free-diffusion process. *Phys. Rev. E*, 76(4):041112, 2007.
- [45] B.E. Griffith. An accurate and efficient method for the incompressible Navier-Stokes equations using the projection method as a preconditioner. *J. Comp. Phys.*, 228(20):7565–7595, 2009.
- [46] A. Donev and E. Vanden-Eijnden. Discrete Fluctuation-Dissipation Balance in Numerical Schemes for Stochastic Conservation Equations. In preparation, 2011.
- [47] P. Español. Stochastic differential equations for non-linear hydrodynamics. *Physica A*, 248(1-2):77–96, 1998.
- [48] R. Kubo. The fluctuation-dissipation theorem. *Reports on Progress in Physics*, 29(1):255–284, 1966.
- [49] H.C. Ottinger. *Beyond equilibrium thermodynamics*. Wiley Online Library, 2005.
- [50] P. Español, J.G. Anero, and I. Zúñiga. Microscopic derivation of discrete hydrodynamics. *J. Chem. Phys.*, 131:244117, 2009.
- [51] D. Bedeaux and P. Mazur. Renormalization of the diffusion coefficient in a fluctuating fluid I. *Physica*, 73:431–458, 1974.
- [52] G. Da Prato. *Kolmogorov equations for stochastic PDEs*. Birkhauser, 2004.
- [53] L.D. Landau and E.M. Lifshitz. *Statistical Physics*, volume 5 of *Course of Theoretical Physics*. Pergamon, third ed., part 1 edition, 1980.
- [54] D. Brogioli and A. Vailati. Diffusive mass transfer by nonequilibrium fluctuations: Fick’s law revisited. *Phys. Rev. E*, 63(1):12105, 2000.
- [55] S. Gottlieb and C. Shu. Total variation diminishing Runge-Kutta schemes. *Mathematics of Computation*, 67(221):73–85, 1998.
- [56] J. B. Bell, P. Colella, and H. M. Glaz. A second order projection method for the incompressible Navier-Stokes equations. *J. Comp. Phys.*, 85(2):257–283, December 1989.
- [57] A. S. Almgren, J. B. Bell, and W. G. Szymczak. A numerical method for the incompressible Navier-Stokes equations based on an approximate projection. *SIAM J. Sci. Comput.*, 17(2):358–369, March 1996.

- [58] E. Weinan and J.G. Liu. Projection method iii: Spatial discretization on the staggered grid. *Mathematics of Computation*, 71(237):27–48, 2002.
- [59] E. Weinan and J.G. Liu. Gauge method for viscous incompressible flows. *Commun. Math. Sci*, 1(2):317–332, 2003.
- [60] P. J. Atzberger. Spatially Adaptive Stochastic Numerical Methods for Intrinsic Fluctuations in Reaction-Diffusion Systems. *J. Comp. Phys.*, 229(9):3474 – 3501, 2010.
- [61] A.S. Almgren, J.B. Bell, and W.Y. Crutchfield. Approximate projection methods: Part i. inviscid analysis. *SIAM Journal on Scientific Computing*, 22:1139, 2000.
- [62] F.H. Harlow and J.E. Welch. Numerical calculation of time-dependent viscous incompressible flow of fluids with free surfaces. *Physics of Fluids*, 8:2182–2189, 1965.
- [63] Y. Morinishi, TS Lund, OV Vasilyev, and P. Moin. Fully conservative higher order finite difference schemes for incompressible flow. *J. Comp. Phys.*, 143(1):90–124, 1998.
- [64] Y. Morinishi. Skew-symmetric form of convective terms and fully conservative finite difference schemes for variable density low-Mach number flows. *J. Comp. Phys.*, 229(2):276–300, 2010.
- [65] J.D. Ramshaw and K. Lindenberg. Augmented langevin description of multiplicative noise and nonlinear dissipation in hamiltonian systems. *J. Stat. Phys*, 45(1):295–307, 1986.
- [66] B.E. Griffith, R.D. Hornung, D.M. McQueen, and C.S. Peskin. An adaptive, formally second order accurate version of the immersed boundary method. *Journal of Computational Physics*, 223(1):10–49, 2007. Software available at <http://ibamr.googlecode.com>.
- [67] R. D. Hornung, A. M. Wissink, and S. R. Kohn. Managing complex data and geometry in parallel structured amr applications. *Engineering with Computers*, 22(3):181–195, 2006. Software available at <https://computation.llnl.gov/casc/SAMRAI>.
- [68] Satish Balay, William D. Gropp, Lois Curfman McInnes, and Barry F. Smith. Efficient management of parallelism in object oriented numerical software libraries. In E. Arge, A. M. Bruaset, and H. P. Langtangen, editors, *Modern Software Tools in Scientific Computing*, pages 163–202. Birkhäuser Press, 1997. Software available at <http://www.mcs.anl.gov/petsc>.
- [69] R. Falgout, J. Jones, and U. Yang. The design and implementation of hypre, a library of parallel high performance preconditioners. *Numerical solution of partial differential equations on parallel computers*, pages 267–294, 2006. Software available at <http://www.llnl.gov/CASC/hypre>.
- [70] J. M. Ortiz de Zárate, F. Peluso, and J. V. Sengers. Nonequilibrium fluctuations in the

- Rayleigh-Bénard problem for binary fluid mixtures. *Euro. Phys. J. E*, 15(3):319–333, 2004.
- [71] T. Alazard. A minicourse on the low Mach number limit. *Discrete Contin. Dyn. Syst. Ser. S*, 1:365–404, 2008.